

# HADES RV programme with HARPS-N at the TNG<sup>★</sup>

## X. A super-Earth around the M dwarf Gl 686

L. Affer<sup>1</sup>, M. Damasso<sup>2</sup>, G. Micela<sup>1</sup>, E. Poretti<sup>3,4</sup>, G. Scandariato<sup>5</sup>, J. Maldonado<sup>1</sup>, A. F. Lanza<sup>5</sup>, E. Covino<sup>6</sup>, A. Garrido Rubio<sup>1</sup>, J. I. González Hernández<sup>7,8</sup>, R. Gratton<sup>9</sup>, G. Leto<sup>5</sup>, A. Maggio<sup>1</sup>, M. Perger<sup>10,11</sup>, A. Sozzetti<sup>2</sup>, A. Suárez Mascareño<sup>7,12</sup>, A. S. Bonomo<sup>2</sup>, F. Borsa<sup>3</sup>, R. Claudi<sup>9</sup>, R. Cosentino<sup>4</sup>, S. Desidera<sup>9</sup>, E. Molinari<sup>13</sup>, M. Pedani<sup>4</sup>, M. Pinamonti<sup>2</sup>, R. Rebolo<sup>7,8</sup>, I. Ribas<sup>10,11</sup>, and B. Toledo Padrón<sup>7,8</sup>

<sup>1</sup> INAF - Osservatorio Astronomico di Palermo, Piazza del Parlamento 1, 90134 Palermo, Italy  
e-mail: laura.affer@inaf.it

<sup>2</sup> INAF - Osservatorio Astrofisico di Torino, via Osservatorio 20, 10025 Pino Torinese, Italy

<sup>3</sup> INAF - Osservatorio Astronomico di Brera, via E. Bianchi 46, 23807 Merate (LC), Italy

<sup>4</sup> INAF - Fundación Galileo Galilei, Rambla José Ana Fernández Pérez 7, 38712, Breña Baja, TF, Spain

<sup>5</sup> INAF - Osservatorio Astrofisico di Catania, via S. Sofia 78, 95123 Catania, Italy

<sup>6</sup> INAF - Osservatorio Astronomico di Napoli, Salita Moiarriello, 16, 80131 Napoli, Italy

<sup>7</sup> Instituto de Astrofísica de Canarias, 38205 La Laguna, Tenerife, Spain

<sup>8</sup> Universidad de La Laguna, Dpto Astrofísica, 38206 La Laguna, Tenerife, Spain

<sup>9</sup> INAF - Osservatorio Astronomico di Padova, Vicolo dell'Osservatorio 5, 35122, Padova, Italy

<sup>10</sup> Institut de Ciències de l'Espai (ICE,CSIC), Campus UAB, Carrer de Can Magrans s/n, 08193 Bellaterra, Spain

<sup>11</sup> Institut d'Estudis Espacials de Catalunya (IEEC), 08034 Barcelona, Spain

<sup>12</sup> Observatoire Astronomique de l'Université de Genève, 1290, Versoix, Switzerland

<sup>13</sup> INAF - Osservatorio Astronomico di Cagliari, Viale della Scienza, 5, 09047 Selargius, Cagliari, Italy

Received 14 December 2018; accepted 13 January 2019

### ABSTRACT

**Aims.** The HARPS-n red Dwarf Exoplanet Survey\*\* is providing a major contribution to the widening of the current statistics of low-mass planets, through the in-depth analysis of precise radial velocity measurements in a narrow range of spectral sub-types. Using the HARPS-N spectrograph we reach the precision needed to detect small planets with a few earth masses. Our survey is mainly focused on the M-dwarf population of the northern hemisphere.

**Methods.** As part of that programme, we obtained radial velocity measurements of Gl 686, an M1 dwarf at  $d = 8.2$  pc. These measurements show a dispersion much in excess of their internal errors. The analysis of data obtained within an intensive observing campaign, demonstrates that the excess dispersion is due to a coherent signal, with a period of 15.53 d. Almost simultaneous photometric observations were carried out within the APACHE and EXORAP programmes to characterize the stellar activity and to distinguish periodic variations related to activity from signals due to the presence of planetary companions, complemented also with ASAS photometric data. We used a Bayesian framework to estimate the orbital parameters and the planet minimum mass, and to properly treat the activity noise. We took advantage of the available radial velocity measurements for this target from other observing campaigns. The analysis of the radial velocity composite time series from the HIRES, HARPS and HARPS-N spectrographs, consisting of 198 measurements taken over 20 years, enabled us to address the nature of periodic signals and also to characterize stellar physical parameters (mass, temperature and rotation).

**Results.** We report the discovery of a super-Earth orbiting at a distance of 0.092 AU from the host star Gl 686. Gl 686 b has a minimum mass of  $7.1 \pm 0.9 M_{\oplus}$  and an orbital period of  $15.532 \pm 0.002 d$ . The analysis of the activity indexes, correlated noise through a Gaussian process framework and photometry, provides an estimate of the stellar rotation period at 37 d, and highlights the variability of the spot configuration during the long timespan covering 20 yrs. The observed periodicities around 2000 d likely point to the existence of an activity cycle.

**Key words.** techniques: radial velocities - techniques: photometric - methods: data analysis - stars: individual: Gl686 - instrumentation: spectrographs - planets and satellites: detection

## 1. INTRODUCTION

Very low-mass stars are very promising targets for planet search programmes, in particular, to discover super-Earths/Earths located in their habitable zone (HZ). Their detection is in principle accessible to the existing spectrographs of highest radial velocity (RV) precision, but it is challenging due to stellar activity which introduces correlated and uncorrelated noise into RV curves (RV jitter). On the other hand, the lower masses

<sup>★</sup> Based on: observations made with the Italian *Telescopio Nazionale Galileo* (TNG), operated on the island of La Palma by the INAF - *Fundación Galileo Galilei* at the *Roche de Los Muchachos* Observatory of the *Instituto de Astrofísica de Canarias* (IAC); photometric observations made with the APACHE array located at the Astronomical Observatory of the Aosta Valley; photometric observations made with the robotic telescope APT2 (within the EXORAP program) located at Serra La Nave on Mt. Etna.

\*\* [http://www.oact.inaf.it/exoit/EXO-IT/Projects/Entries/2011/12/27\\_GAPS.html](http://www.oact.inaf.it/exoit/EXO-IT/Projects/Entries/2011/12/27_GAPS.html)

of M dwarfs result in a higher Doppler wobble RV amplitude for a given planetary mass, and the low luminosities of M dwarfs imply that the boundaries of their HZ are located at short separations (typically between 0.02 AU and 0.2 AU, see, e.g., Mandell et al. 2007), making habitable rocky planets more easy to detect with present-day observing facilities than those around more massive stars (e.g., Tuomi et al. 2014; Charbonneau & Deming 2007). The most recent evidence gathered by RV surveys and ground-based as well as space-borne transit search programmes points toward the ubiquitousness of low-mass companions with small radii around M dwarfs (e.g., Sozzetti et al. 2013; Crossfield et al. 2015; Dressing & Charbonneau 2015). The number of confirmed planets is steadily growing and in recent years many planetary systems hosting Neptune mass planets (e.g., Howard et al. 2014; Astudillo-Defru et al. 2015) and super-Earths (e.g., Delfosse et al. 2013; Ribas et al. 2018) have been reported and Earth-mass planets, as well (e.g., Anglada-Escudé et al. 2016; Gillon et al. 2017; Astudillo-Defru et al. 2017b). Nevertheless, the frequency statistics of low-mass planets hosted by low-mass stars remains poorly constrained. Several studies have attempted to quantify the abundance of rocky planets in close orbits and in the habitable zones of M dwarfs, but the uncertainties are still large, making it important to continue adding new planets to the sample (Bonfils et al. 2013; Gaidos 2013; Dressing & Charbonneau 2015).

We present high-precision, high-resolution spectroscopic measurements of the bright M1 dwarf Gl686, gathered with the HARPS-N spectrograph (Cosentino et al. 2012) on the Telescopio Nazionale Galileo (TNG) as part of the HARPS-n red Dwarf Exoplanet Survey (HADES), described in detail in Affer et al. (2016). The HADES collaboration has already produced several valuable results, regarding both the statistic/activity/characterization of M stars (Perger et al. 2017a; Maldonado et al. 2017; Scandariato et al. 2017; Maldonado et al. 2015; Suárez Mascareño et al. 2018), and the planet discovery (Affer et al. 2016; Suárez Mascareño et al. 2017; Perger et al. 2017b; Pinamonti et al. 2018).

For the study of Gl686 we also took advantage of archive observations with the HARPS and HIRES spectrographs, as part of other observing campaigns. In Sect. 2 we summarize the atmospheric, physical, and kinematic properties of Gl686. In Sect. 3 we describe the data-sets and the RV analysis and discuss the effect of stellar activity, for the time series of every single instrument and for the composite time series. Section 4 presents the analysis and results of a multi-site photometric monitoring campaign. In Sect. 5 we describe the Bayesian analysis and the model selection and derive the system parameters. In Sect. 6 we discuss our results, and we summarize our findings and conclude in Sect. 7.

## 2. STELLAR PROPERTIES OF Gl 686

Gl686 is a variable dwarf at a distance of 8 pc from the Sun. The rotation period of Gl686 has been estimated by Suárez Mascareño et al. (2018), within the HADES programme using 9 HARPS-N and 20 HARPS spectra (see Suárez Mascareño et al. 2018 for details on the method), though a direct determination was not possible, the expected rotation period is  $70 \pm 12$  d. Astudillo-Defru et al. (2017a) estimated a rotation period of 55 d for Gl686, using only the HARPS data.

Accurate stellar parameters were determined using the empirical

**Table 1.** Stellar parameters for the star Gl686 from the analysis of the HARPS-N spectra using the technique in Maldonado et al. (2015) (in the upper part, except for the  $\log R'_{\text{HK}}$  value, calculated by Suárez Mascareño et al. 2018). In the lower part of the table coordinates, V and K magnitudes, parallax, proper motions and space velocities are indicated.

Parameter <sup>(5)</sup>	Gl 686
Spectral Type	M1
$T_{\text{eff}}$ [K]	$3663 \pm 68$
[Fe/H] [dex]	$-0.30 \pm 0.09$
Mass [ $M_{\odot}$ ]	$0.42 \pm 0.05$
Radius [ $R_{\odot}$ ]	$0.42 \pm 0.05$
$\log g$ [cgs]	$4.83 \pm 0.04$
Luminosity [ $L_{\star}/L_{\odot}$ ]	$0.028 \pm 0.006$
$v \sin i$ [ $\text{km s}^{-1}$ ]	$1.01 \pm 0.80$
$\log R'_{\text{HK}}$ <sup>(1)</sup>	$-5.42 \pm 0.05$
$\alpha$ (J2000)	$17^{\text{h}}:37^{\text{m}}:52.8^{\text{s}}$
$\delta$ (J2000)	$+18^{\circ}:35':21''$
$V_{\text{mag}}$ <sup>(2)</sup>	9.577
$K_{\text{mag}}$ <sup>(3)</sup>	5.572
$\pi$ [mas] <sup>(4)</sup>	$122.56 \pm 0.03$
$\mu_{\alpha}$ [mas/yr] <sup>(4)</sup>	$926.74 \pm 0.05$
$\mu_{\delta}$ [mas/yr] <sup>(4)</sup>	$984.70 \pm 0.07$
$U_{\text{LSR}}$ [ $\text{km s}^{-1}$ ] <sup>(5)</sup>	$-24.4 \pm 0.4$
$V_{\text{LSR}}$ [ $\text{km s}^{-1}$ ] <sup>(5)</sup>	$40.2 \pm 0.6$
$W_{\text{LSR}}$ [ $\text{km s}^{-1}$ ] <sup>(5)</sup>	$-13.9 \pm 0.4$
S [ $\text{km s}^{-1}$ ] <sup>(5)</sup>	$49.0 \pm 0.6$

References. <sup>(1)</sup> Suárez Mascareño et al. (2018); <sup>(2)</sup> Koen et al. (2010); <sup>(3)</sup> Cutri et al. (2003); <sup>(4)</sup> Gaia Collaboration et al. (2016); Gaia Collaboration (2018); <sup>(5)</sup> This work (see text).

relations by Maldonado et al. (2015)<sup>1</sup> on the same HARPS-N spectra used in the present work to derive RVs (see Table 1). Stars presently near the Sun may come from a wide range of Galactic locations. Therefore, stellar space velocity, as a clue to the origin of a star in the Galaxy, is very important. The accurate *Gaia* parallax (Gaia Collaboration et al. 2016; Gaia Collaboration 2018), combined with the proper motions and the stellar radial velocity, makes it possible to derive reliable space velocities for Gl686. All kinematic data and stellar properties are listed in Table 1. We have calculated the probabilities that the star belongs to a specific population, thick (TD), thin disk (D) or stellar halo (H), following the method used by Bensby et al. (2004). On account of these probabilities, we find for Gl686 a thick-disk to thin-disk probability ratio of  $TD/D = 0.07$ , implying that the star is clearly identified as a thin-disk object (typical threshold for assignment to thin disk being  $TD/D < 0.1$ , Bensby et al. 2004).

## 3. DATA-SETS AND ANALYSIS

### 3.1. Data

During the last 20 yrs, Gl686 has been monitored by three different surveys and instruments, as detailed below:

- from BJD = 2 450 604.9 (June 5, 1997) to BJD = 2 456 551.8 (September 16, 2013), using the optical echelle HIRES spectrograph on the Keck-I telescope within the survey carried out by the Lick-Carnegie Exoplanet Survey Team (LCES),

<sup>1</sup> <http://www.astropa.inaf.it/~jmalonado/Msdlines.html>

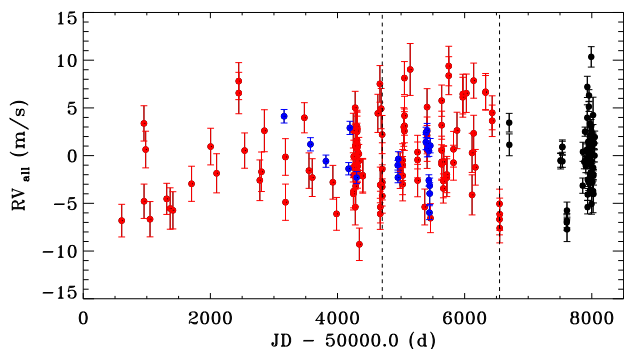


**Fig. 1.** Composite radial velocity time serie from HIRES (red), HARPS (blue) and HARPS-N (black), for Gl 686, after offset correction. The two vertical lines indicate the separation between the different *seasons*, composed by an equal number of data points (66 data points each).

obtaining 114 spectra at high resolution (archive public data). For HIRES data we used the RVs measured by Butler et al. (2017), taking into account the recent correction by Tal-Or et al. (2018).

- from BJD = 2 453 159.7 (June 3, 2004) to BJD = 2 455 458.5 (September 19, 2010), using the optical echelle HARPS spectrograph on the ESO La Silla telescope (Mayor et al. 2003), obtaining 20 spectra at high resolution (archive public data).
- from BJD = 2 456 700.7 (February 12, 2014) to BJD = 2 458 047.3 (October 20, 2017), using the HARPS-N spectrograph on the TNG telescope, as part of the HADES programme.

The spectra were obtained at high resolution with exposure times of 15 minutes and average signal-to-noise ratio (S/N) of 75 at 5500 Å. Of the 64 HARPS-N epochs, 49 were obtained within the GAPS observing programme and 15 within the Spanish observing programme. Observations were gathered without the simultaneous Th-Ar calibration, which is usually used to correct for instrumental drifts during the night. Perger et al. (2017a) demonstrated that we can account for the lack of inter-night instrumental drift adding quadratically a mean instrumental drift of  $1 \text{ m s}^{-1}$  to the RV uncertainties. This choice avoided the contamination of the Ca II H & K lines, which are particularly important for the stellar activity analysis of M dwarfs (Giampapa et al. 1989; Forveille et al. 2009; Lovis et al. 2011).

The information on data-sets, instruments and surveys used in the present work, are summarized in Table 2. The RV time series for HARPS and HARPS-N are provided in in Table A.1.

**Table 2.** Information on the data-sets and instruments used in the present work.

Survey	Telescope/ Instrument	Resolving Power	Time-span $\Delta T$ (d)	#Data points
HADES	TNG/HARPS-N	115 000	1347	64
LCES	Keck-I/HIRES	60 000	5947	114
HMDS <sup>(*)</sup>	ESO/HARPS	115 000	2299	20

<sup>(\*)</sup>: The HARPS M dwarf sample; program IDs: 072.C-0488, 183.C-0437.

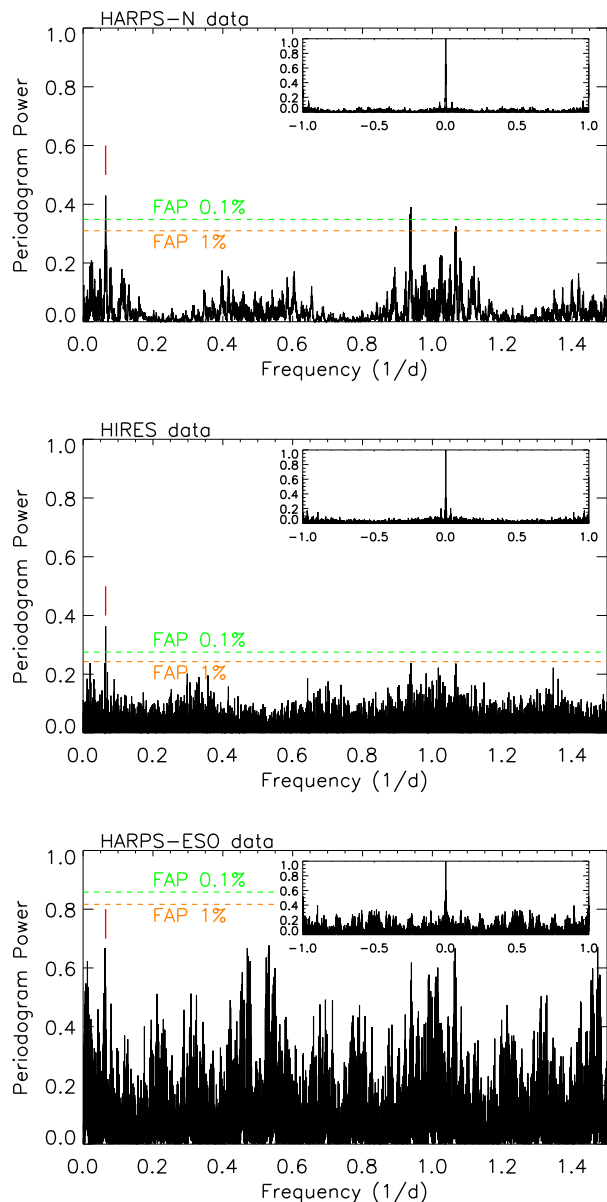


**Fig. 2.** Power spectrum of the HARPS-N, HIRES, HARPS data, from top to bottom, with the spectral window in insets. The period at 15.5 d is indicated with a red mark.

### 3.2. RV Period Search

We performed the same analysis on the three datasets separately, and on the composite dataset, including RV measurements from the three spectrographs. Joining the three different datasets, we obtained a total of 198 data points (114 HIRES - 20 HARPS - 64 HARPS-N) spanning more than 7400 days, with HIRES and HARPS data overlapping. When we consider the RV data of the three different spectrographs, HIRES, HARPS and HARPS-N, we need to compensate for the instrument offset of the different measurements. This is done with the IDL programme *RVlin.pro* (Wright & Howard 2009). Once the offset is calculated, the RV measurements of two instruments (here HIRES, and HARPS) can be corrected for it and be brought to the same zero-point as the HARPS-N measurements (Fig. 1).

HARPS-N data reduction and spectral extraction were performed using the Data Reduction Software (DRS v3.7, Lovis &

Pepe 2007). RVs were measured by matching the spectra with a high S/N template obtained by co-adding the spectra of the target, as implemented in the TERRA pipeline (Anglada-Escudé & Butler 2012). This strategy provides a better RV accuracy when applied to M-dwarfs, as shown in Perger et al. (2017a). We employed the same approach to measure the RVs also for HARPS data.

The TERRA pipeline performs the correction for the secular acceleration (Kürster et al. 2003), and the RV dataset from the Keck archive was already corrected for the secular acceleration of the host star ( $0.34 \text{ m s}^{-1} \text{ yr}^{-1}$ ).

The first step of the RV data analysis consists in identifying significant periodic signals in the data. Pre-whitening is a commonly used tool for finding multi-periodic signals in time series data. With this method we find sequentially the dominant Fourier components in the time series and remove them. The pre-whitening procedure was applied to the RV data using the Generalized Lomb-Scargle (GLS) periodogram algorithm (Zechmeister & Kürster 2009) and the programme *Period04* (Lenz & Breger 2004), for an independent test. We calculated the false alarm probabilities (FAP) of detection using 10 000 bootstrap randomization (Endl et al. 2001) of the original RV time series. Once a significant peak was located at a given period, the corresponding sinusoidal function was adjusted and removed. The process was repeated several times until no significant peak remained. The two methods yielded the same results in terms of extracted frequencies from our RV time series.

**HARPS – N** – The RVs show a root mean square (RMS) dispersion of  $3.16 \text{ m s}^{-1}$  and a mean formal error of  $0.82 \text{ m s}^{-1}$  ( $1.3 \text{ m s}^{-1}$ , adding quadratically the mean instrumental drift of  $1 \text{ m s}^{-1}$  to the RV uncertainties). The GLS periodogram indicates as significant (FAP 1%) a period of  $15.52 \pm 0.01 \text{ d}$ , the residuals time series has a RMS of  $2.42 \text{ m s}^{-1}$  and a significant period of  $36.7 \pm 0.1 \text{ d}$ . The time series obtained eliminating these two significant periods has a RMS of  $2.0 \text{ m s}^{-1}$  and a period of  $12.95 \pm 0.02 \text{ d}$ , which is not significant at the 1% FAP threshold.

**HARPS** – The RVs show a RMS dispersion of  $2.52 \text{ m s}^{-1}$  and a mean error of  $1.22 \text{ m s}^{-1}$ . The GLS periodogram indicates a period of  $15.96 \pm 0.01 \text{ d}$ , the residuals time series has a RMS of  $1.41 \text{ m s}^{-1}$  and a period of  $4.4947 \pm 0.0007 \text{ d}$ , both periods are not significant.

**HIRES** – The RVs show a RMS dispersion of  $4.09 \text{ m s}^{-1}$  and a mean error of  $1.84 \text{ m s}^{-1}$ . The GLS periodogram indicates a significant period of  $15.53 \pm 0.003 \text{ d}$ , the residuals time series has a RMS of  $3.3 \text{ m s}^{-1}$  and a significant period of  $49.09 \pm 0.04 \text{ d}$ . The time series obtained eliminating these two significant periods has a RMS of  $2.8 \text{ m s}^{-1}$  and a not significant period of  $30.3 \pm 0.02 \text{ d}$ .

The GLS periodogram of the three datasets is shown in Fig. 2, the 0.1% and 1% FAP levels are shown as dashed lines, the window functions are plotted in insets for each instrument.

**HIRES + HARPS + HARPS – N** – The RVs show a RMS dispersion of  $3.45 \text{ m s}^{-1}$  and a mean error of  $1.51 \text{ m s}^{-1}$ , the GLS periodogram (with a period search extended to 3 700 d, due to the long timespan of the composite observations) indicates a significant period of  $15.531 \pm 0.001 \text{ d}$  with a very high spectral power, the residuals time series has a RMS of  $3.07 \text{ m s}^{-1}$  and a significant period of  $45.95 \pm 0.03 \text{ d}$ . The time series obtained eliminating these two significant periods has a RMS of  $2.9 \text{ m s}^{-1}$  and a significant period of  $31.35 \pm 0.01 \text{ d}$ . The GLS periodogram of the complete dataset is shown in Fig. 3, the

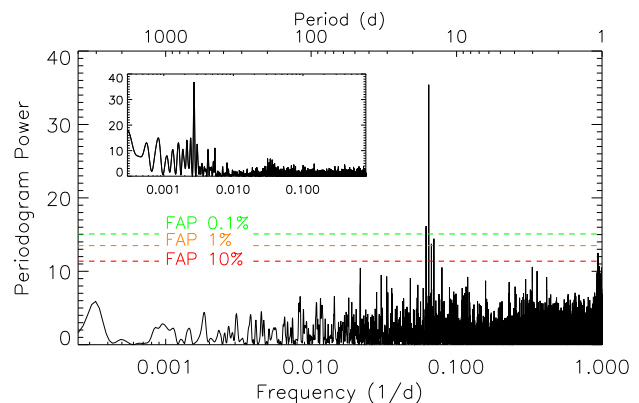


**Fig. 3.** GLS periodogram of the complete dataset (HIRES+HARPS+HARPS-N). The dashed lines indicate 0.1%, 1% and 10% levels of false alarm probability. The spectral window is shown in inset, the highest peak is related to the 1-year alias.

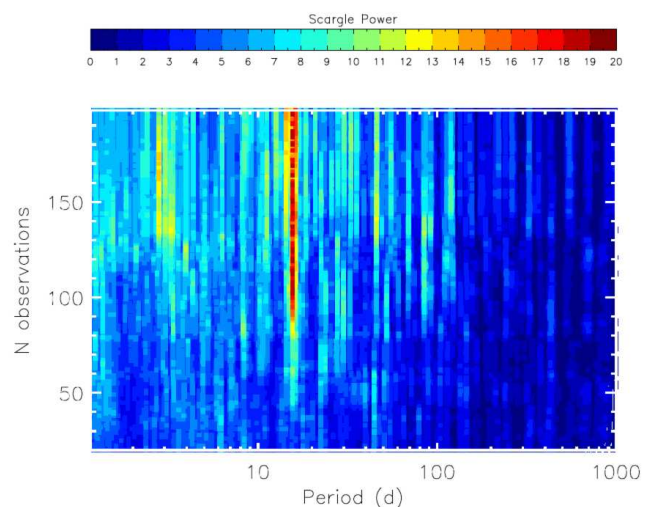


**Fig. 4.** Periodogram power of the inspected periods as a function of the number of observations. The most significant period (the reddest one) at 15.5 d is clearly visible with a high power for  $N_{obs} > 80$ , as well as a period around 3 d with a moderate Scargle power, which increases for  $N_{obs} > 160$  and then decreases again as well as a period between 40 and 50 d.

0.1%, 1% and 10% FAP levels are shown as dashed lines.

To visualize the cumulative contribution of data points to the significance of the detected frequencies, we calculated the GLS periodograms increasing the number of observations (Mortier & Collier Cameron 2017), from 20 to  $N_{tot}$ , adding one observation at a time (following the exact order of data acquisition), the result is shown in Fig. 4. We compute the power corresponding to each of the periods in the range 1.2 d to  $P_{Max} = (T_{BJD_{Max}} - T_{BJD_{Min}})/2.0$ , for each periodogram obtained. Each horizontal slice of Fig. 4 gives powers (indicated by the color scale) versus periods for the periodogram corresponding to the observations number, indicated on the vertical axis. Fig. 4 is a 2D representation of the technique applied to the complete G1686 dataset (HARPS-N+HARPS+HIRES).

We also performed a different analysis by using the iterative sine-wave fitting least-squares method (Vaníček 1971). This approach is used in the asteroseismic analysis of multiperiodic

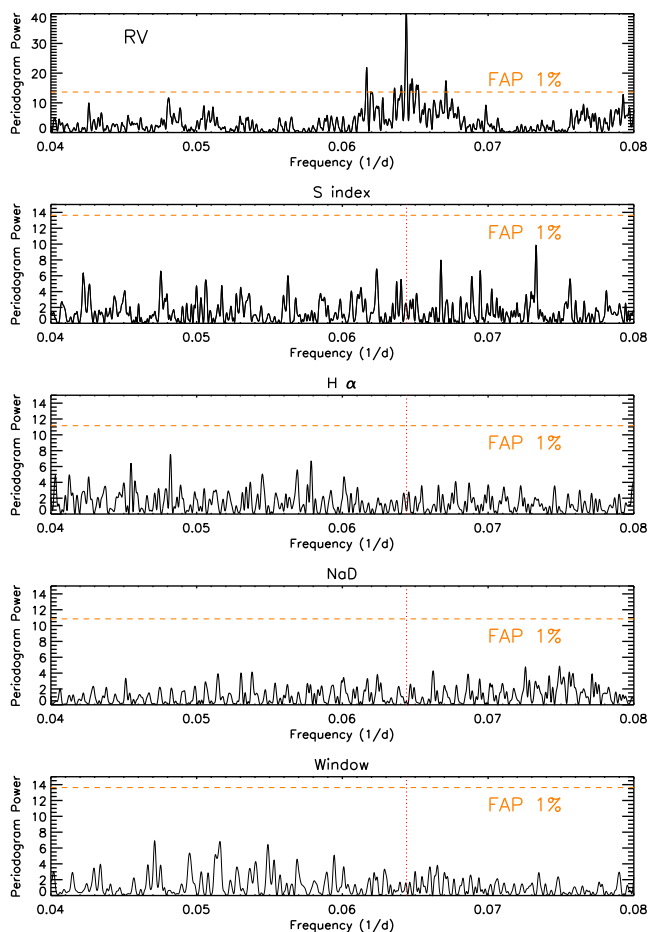


**Fig. 5.** GLS periodograms around the period of 15.5 d (from top to bottom): RV (HIRES+HARPS+HARPS-N), Sindex (HIRES+HARPS+HARPS-N),  $H\alpha$  (HARPS+HARPS-N), NaD (HARPS+HARPS-N) and window function. The 15.5 d period is indicated in each periodogram, as the red dashed line.

pulsating stars to minimize the subtle effects of pre-whitening, such as power exchange between a signal frequency and an alias of another signal frequency. After each detection, only the frequency values were introduced as known parameters in the new search. In this way, their amplitudes and phases were recalculated for each new trial frequency, always subtracting the exact amount of signal for any known periodicity. This new analysis again confirmed the previously determined frequencies.

### 3.3. Aliases: connection to window function peaks

A careful analysis of the spectral window, following the methods of Dawson & Fabrycky (2010), ruled out that the peak at 15.5 d in the periodograms is an artifact due to the combination of the activity with the spectral window (or to the time sampling alone).

By taking a closer look at the RV and window function periodograms (Fig. 2), it is clearly visible that the window function does not show significant peaks at the same frequency as the RV periodogram. In particular, since the window function is superimposed at every real frequency, overplotting the window function at the most prominent peaks found in the RV periodogram allows us to see how the ancillary peaks (on both sides) of the

real frequency are caused purely by the sampling function (in particular yearly aliases).

### 3.4. Stellar Activity

To investigate RV variability against stellar activity, we make use of spectral indexes based on Ca II H&K ( $S$ -index),  $H\alpha$  and NaD lines, obtained as results of the TERRA pipeline for HARPS-N and HARPS data, and  $S$ -index and  $H\alpha$  available from the Keck archive, for this target (Fig. A.1). The index based on NaD lines was defined following the receipt of Maldonado et al. (2015) for Ca II H&K lines.

The average Ca II H&K activity index  $R'_{\text{HK}}$ , measured by Suárez Mascareño et al. (2018) (Table 1), indicates a low chromospheric activity level for Gl 686.

**HARPS – N –** The GLS periodogram for  $H\alpha$  time series (Fig. A.3), indicates a significant period of  $37.05 \pm 0.07$  d; no significant peaks for NaD; the significant periodicity observed for  $S$  index, is related to the 1-year alias.

**HARPS –** None of the peaks found in the GLS periodogram of activity indexes of HARPS data is significant.

**HIRES –** The GLS periodogram for  $H\alpha$  time series (Fig. A.3) indicates a significant period of  $45.35 \pm 0.05$  d; a significant period of  $38.00 \pm 0.02$  d for  $S$ -index.

We performed the activity analysis also for the composite time series obtained by joining the indexes of the three different datasets. For what concerns the measurements of  $H\alpha$  and NaD, we used only the HARPS and HARPS-N data for which we were able to obtain homogeneous measures (the HIRES  $H\alpha$  values cover a different scale).

**HIRES + HARPS + HARPS – N –** The GLS periodogram for  $S$ -index (Fig. A.4) indicates a long significant period of  $2267 \pm 50$  d.

**HARPS + HARPS – N –** The GLS periodogram for  $H\alpha$  indicates a significant period of  $2500 \pm 49$  d, the residuals time series has a significant period of  $40.83 \pm 0.03$  d; no significant period was observed for NaD.

The period of 40.8 d is the 1-yr alias of the 37 d rotation period, the last one is the second significant peak in the  $H\alpha$  periodogram shown in Fig. A.4. Removing the long 2500 d period, both the periods gain power, with the alias one growing in power more than the physical rotation period.

These periodicities around 2000 d are apparent also in the whole RV time series in Fig. 1. They indicate that the long-term modulation of the RV is very likely associated with an activity cycle. This period is consistent with those observed for other similar objects (see, for example, Fig. 11 in Suárez Mascareño et al. 2018).

In the analysis of the activity indicators (when available in the different datasets), no periodic variations around 15.53 d were observed in the  $S$ -index,  $H\alpha$  and NaD time series, nor in the spectral window.

In Fig. 5 we show the periodograms of RV data, activity indexes and spectral window zoomed around the frequency of interest ( $f=0.064 \text{ d}^{-1} - P = 15.53 \text{ d}$ ), while in Fig. 6 we show the 2D representation of the GLS analysis, the periodogram power of the inspected periods of the  $S$ -index and  $H\alpha$  time series, as a function of the number of observations. There are several significant periods larger than 100 d, probably due to long trends and a series of significant periods between 29 d and 40 d, for  $S$ -index and around 40 d, for  $H\alpha$ .

The significant periods of the activity indexes, highlighted by

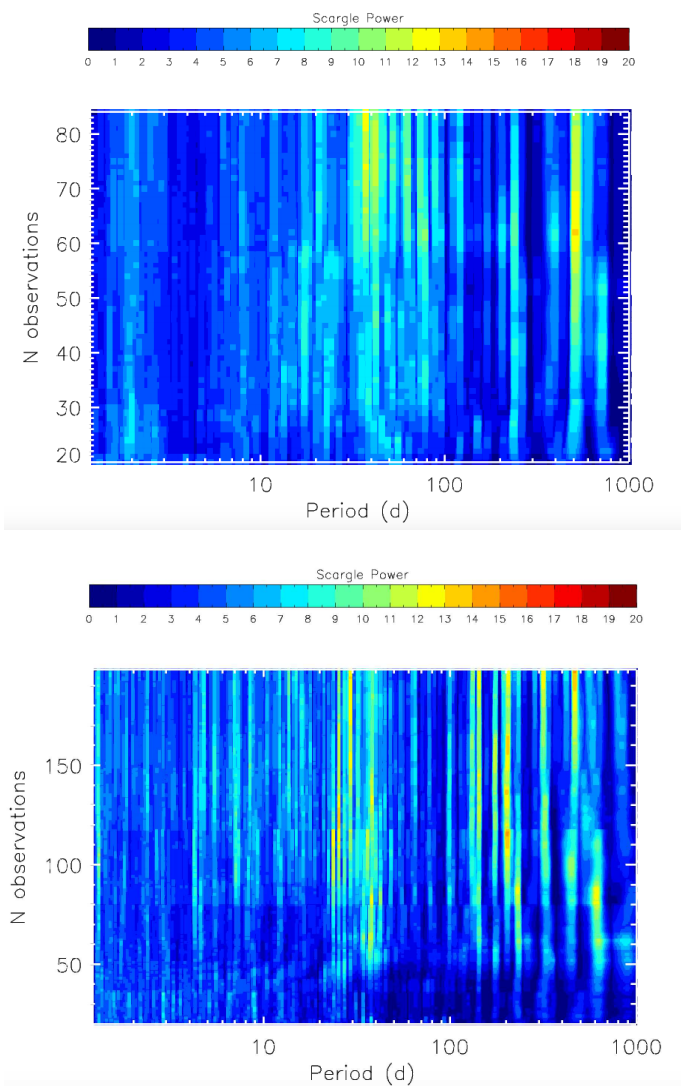


**Fig. 6.** Periodogram power of the inspected periods as a function of the number of observations for the  $H\alpha$  (top panel) and  $S$ -index (bottom panel) time series. There are several significant periods larger than 100 d, probably due to long trends and a series of significant periods between 27 d and 42 d, for  $S$  index and around 40 d, for  $H\alpha$ .

the GLS periodogram analysis, are summarized in Table 3, phase folded plots at those periods are shown in Figs. A.5, A.6.

To avoid any misinterpretation of the stellar activity as a planetary signal, we analyzed the combined RV data subdividing it in three consecutive subsets containing an equal number of measurements (66 data points each observing season), to check the persistence of the planetary signal over time and to mitigate the possible effects of discontinuities in the data sampling. In the upper plots of Fig. 7 we show the GLS periodograms zoomed around the frequency ranges of interest for the three seasons. The red, blue and green lines show the first, second and third subset, respectively. In the lower plots we can compare the GLS periodograms for the three telescope datasets, red (HIRES), blue (HARPS) and green (HARPS-N). In the plot we indicate the frequencies obtained from the RV and activity indexes/photometric analysis (see Sect. 4). The periods related to activity effects span a range from 29 to 45 d (Fig. 6), significant peaks in the GLS of several activity indicators, are not stable during the seasons (37, 38, 40 and 45 d in the three seasons/telescope datasets),

and in particular a period of 37 d and 37.8 d is indicated by the Gaussian Process (see Sect. 5) and ASAS photometry (see Sect. 4), respectively, as an estimate of the rotation period. Among the periods identified in the stellar activity indicators, only the period at 36.7 d appears at significant power in RV. We attribute this periodicity to the rotation period of the star.

The feature at  $P = 15.53$  d ( $f = 0.064$  d $^{-1}$ ) is observed in the three seasons, as the most significant period. The RV amplitudes in the three seasons are:  $K_1 = 2.7 \pm 0.5$  m s $^{-1}$  (with phase 0.40),  $K_2 = 3.6 \pm 0.5$  m s $^{-1}$  (with phase 0.40) and  $K_3 = 3.1 \pm 0.4$  m s $^{-1}$  (with phase 0.54), showing the stability of the signal. We notice that the first season is dominated by HIRES RVs, which are less precise than HARPS/HARPS-N ones, and this reflects in the RV amplitude  $K_1$  and periodogram power both smaller than in the other two seasons, with the same number of data points. This constitutes further evidence that this signal is present in the RVs at any time (in a time range of more than 20 yrs), leading us to conclude that it has a planetary origin.

We computed the correlation between activity indexes and RV time series via the Spearman's rank correlation coefficients. No significant correlation was identified ( $\rho = -0.01$  for  $S$ -index and  $\rho = -0.34$  for  $H\alpha$ ). We also removed the activity contribution at 36.7 d (adjusting and removing a sinusoidal function with this period) from the RV time series obtaining  $\rho = -0.01$  for  $S$ -index and  $\rho = -0.24$  for  $H\alpha$ , thus we do not identify a correlation that would be expected if the radial velocity variation were still induced by activity features on the star surface.

## 4. PHOTOMETRY

The targets of the HADES programme are photometrically monitored by two independent programmes: APACHE and EXORAP (see Affer et al. 2016, for details on instrumental setup and data reduction). These two programmes regularly follow up the sample of M stars to provide an estimate of the stellar rotation periods by detecting periodic modulation in the differential light curves.

For G1 686 we took advantage also of archive photometric data from ASAS survey.

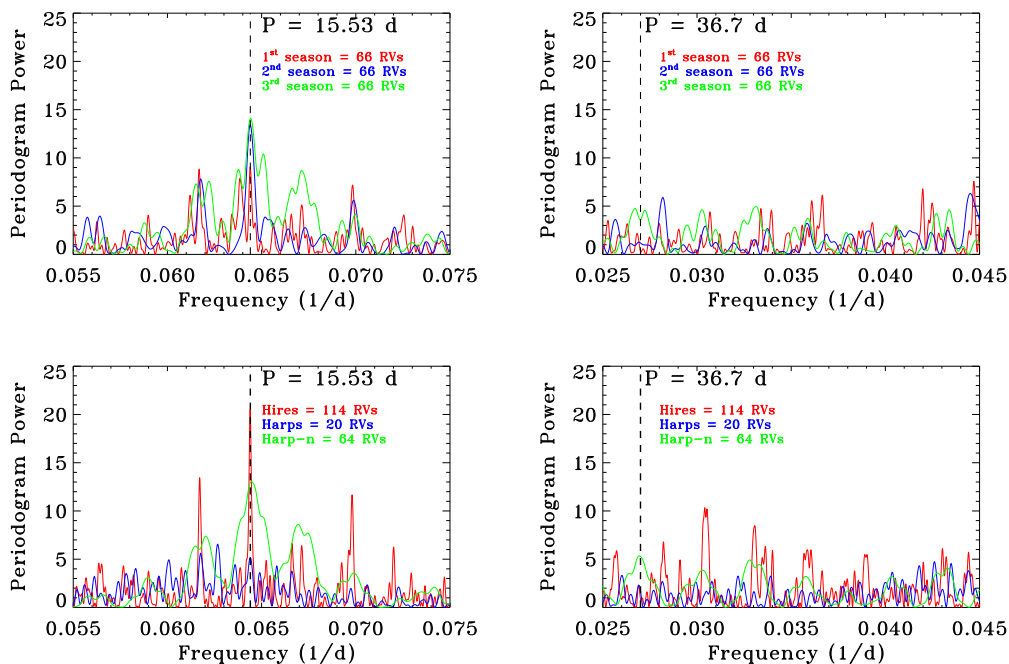
### 4.1. EXORAP photometry

The star G1 686 was monitored at INAF-Catania Astrophysical Observatory with an 80cm f/8 Ritchey-Chretien robotic telescope (APT2) located at Serra la Nave (+14.973°E, +37.692°N, 1725 m a.s.l.) on Mt. Etna. We collected  $BVR$  photometry of G1 686 obtaining 88 data points between 5 May and 18 October 2017. We used aperture photometry as implemented in the IDL routine *aper.pro*, trying a range of apertures to minimize the rms of the ensemble stars. To measure the differential photometry, we started with an ensemble of about six stars, the nearest and brightest to G1 686, and checked the variability of each by building their differential light curves using the remaining ensemble stars as reference. With this method we selected the least variable stars of the sample, typically four. The photometric variability in the  $BVR$  bands is 0.01-0.02 mag, at the level of the night-to-night photometric precision of the survey (Fig. A.2).

The differential photometry of the target was analyzed using the GLS algorithm. No data were rejected after evaluation for outliers (clip at  $5\sigma$ ). For each band, we analyzed the periodograms, assigning them a FAP using the bootstrap method with 10 000

**Table 3.** Significant periods (FAP < 1%) of the activity indexes, obtained with the GLS analysis (pre-whitening). The numbers in brackets indicate the data points of the respective time series.

	<i>S</i> -index	H $\alpha$
a HARPS-N (64)	-	$37.05 \pm 0.7 d$
b HARPS (20)	-	-
c HIRES (114)	$38.00 \pm 0.02 d$	$45.35 \pm 0.05 d$
a+b (84)	-	$2500 \pm 49 d$
		$40.83 \pm 0.03 d$
a+b+c (198)	$2267 \pm 50 d$	-

**Fig. 7.** GLS periodograms around the frequency ranges of interest. The two upper panels refer to three equal subsets of the composite RV data. All the seasons have 66 data points, the first season is shown with a red periodogram, the second season is plotted in blue and the third in green. The two lower panels refer to the separate telescope RV datasets. The HIRES data are shown with a red periodogram, the HARPS periodogram is plotted in blue and the HARPS-N in green. The left panels refer to the frequency related to the candidate planet ( $f = 0.064 d^{-1} - P = 15.53 d$ ). The right panels refer to the frequency related to activity ( $f = 0.027 d^{-1} - P = 36.7 d$ ), as suggested from RV analysis, Gaussian Processes as well as by several activity indicators and ASAS photometry.

iterations. The periodograms of the *B*, *V* and *R* magnitudes do not show any peak above the 5% significance level.

#### 4.2. APACHE photometry

APACHE is a photometric survey devised to detect transiting planets around hundreds of early-to-mid-M dwarfs (Sozzetti et al. 2013). Gl 686 was monitored for 49 nights between March 3, 2015 and June 30, 2016 with one of the five 40cm telescopes composing the APACHE array, located at the Astronomical Observatory of the Autonomous Region of the Aosta Valley (OAVdA, +45.7895 N, +7.478 E, 1650 m.a.s.l.).

The APACHE data were obtained by using an aperture of 4.5 pixels and a set of four comparison stars. We searched the light curve for sinusoidal-like modulation by using the complete dataset consisting of 555 points, each being the average of three consecutive measurements with an uncertainty equal to their rms. The APACHE data show a long-term trend. We used the GLS algorithm to calculate the frequency periodograms. To esti-

mate the significance of the detection, we performed a bootstrap analysis (with replacement) by using 10 000 permuted datasets derived from the original photometric data. The best photometric frequency we find is associated to a period of 29 d in the original dataset and 27 d in the detrended dataset (with a FAP  $\leq 10\%$ ), both of them are close to those found in the RVs and spectroscopic activity index time series, whose power is not significant.

#### 4.3. ASAS photometry

We also analyzed photometry of Gl 686 from the All-Sky Automated Survey (ASAS Pojmanski 1997), which overlaps with HIRES and HARPS data, from March 3, 2003 and May 17, 2009, finding evidence of the stellar rotation period at  $P_{rot} = 37.79 \pm 0.08 d$ . This value is compatible to the stellar rotation period also found in the HARPS-N RV data (36.7 d) and in the activity indicators (37 d in H $\alpha$  and 38 d in *S* index).

We used an autocorrelation analysis (Box & Jenkins 1976; Edel-

**Table 4.** Best-fit values for the parameters of the global model (one planet on a circular orbit + stellar activity) selected as explained in Sect. 5. They are calculated as medians of the marginal posterior distributions, and the uncertainties represent their 16% and 84% quantiles, unless otherwise indicated. The priors used in our MC fitting are also shown. The difference  $\Delta \ln \mathcal{Z}$  between the Bayesian evidence for this model and the one for a 'null' model not including a planet is  $\Delta \ln \mathcal{Z} = -508.37 + 530.68 = 22.31$ , which indicates decisive evidence in favor of the one planet model according to Kass & Raftery (1995). For the 'null' model we have fitted the data only through a GP quasi-periodic regression, using the same priors for the hyper-parameters as for the one planet model.

Parameter (planet)	Value	Prior
$K_b$ [m s <sup>-1</sup> ]	$3.29^{+0.31}_{-0.32}$	$\mathcal{U}(0,20)$
$P_b$ [days]	$15.53209^{+0.00166}_{-0.00167}$	$\mathcal{U}(13.5, 17.5)$
$T_{0,b}$ [BJD-2, 450, 000]	$7805.69^{+0.28}_{-0.27}$	$\mathcal{U}(7800, 7820)$
$e$	0 (fixed)	-
(hyper)parameter (stellar activity)	Value	Prior
$h_{\text{HARPS}}$ [m s <sup>-1</sup> ]	$1.76^{+0.31}_{-0.28}$	$\mathcal{U}(0,20)$
$h_{\text{HIRES}}$ [m s <sup>-1</sup> ]	$3.16^{+0.44}_{-0.40}$	$\mathcal{U}(0,20)$
$\lambda$ [days]	$23.3^{+30.2}_{-18.2}$	$\log \lambda \mathcal{U}(0,3.9)$
$w$	$0.49^{+0.31}_{-0.18}$	$\mathcal{U}(0,1)$
$\theta$ [days]	$37.0^{+5.4}_{-14.4}$	$\mathcal{U}(0, 50)$
$offset_{\text{HARPS-N}}$ [m s <sup>-1</sup> ]	$-0.41^{+0.53}_{-0.62}$	$\mathcal{U}(-100, 100)$
$\sigma_{\text{jitter,HARPS-N}}$ [m s <sup>-1</sup> ]	$1.44^{+0.29}_{-0.26}$	$\mathcal{U}(0, 10)$
$offset_{\text{HARPS}}$ [m s <sup>-1</sup> ]	$-0.33^{+0.60}_{-0.60}$	$\mathcal{U}(-100, 100)$
$\sigma_{\text{jitter,HARPS}}$ [m s <sup>-1</sup> ]	$0.67^{+0.47}_{-0.41}$	$\mathcal{U}(0, 10)$
$offset_{\text{HIRES}}$ [m s <sup>-1</sup> ]	$0.65^{+0.51}_{-0.48}$	$\mathcal{U}(-100, 100)$
$\sigma_{\text{jitter,HIRES}}$ [m s <sup>-1</sup> ]	$0.51^{+0.47}_{-0.35}$	$\mathcal{U}(0, 10)$
Derived quantities		
$M_b \sin i$ [ $M_{\oplus}$ ]	$7.1 \pm 0.9$	
$a_b$ [AU]	$0.091 \pm 0.004$	
$T_{\text{eq,b}}$ [K]	$379^{+24}_{-25}$	

**Notes.** The symbol  $\mathcal{U}(\cdot, \cdot)$  denotes an uninformative prior with corresponding lower and upper limits. The equilibrium temperature  $T_{\text{eq,b}}$  has been derived by assuming Bond albedo  $A_B=0$ .

son & Krolik 1988), only to confirm the periodicity of the ASAS light curve. The time series is random if it consists of a series of independent observations with the same distribution. In this case we would expect the autocorrelation of the time series to be statistically not significant for all values of the lag. The ASAS light curve has an autocorrelation coefficient relative to a period of 36 d significant at  $2\sigma$  level (i.e. the periodogram and autocorrelation analysis agree, within the error bars).

## 5. MONTE CARLO ANALYSIS OF THE RV TIME SERIES BASED ON GAUSSIAN PROCESS REGRESSION

To mitigate the stellar activity signal in the RV time series, and to test the statistical significance of a dynamical model including one planet over the 'null hypothesis' case, where only an activity term is considered, we have defined a Bayesian framework based on a Monte Carlo (MC) sampling of the parameter space. The stellar activity term has been treated as a quasi-periodic signal through a Gaussian process (GP) regression, a technique com-

monly used to detect or characterize many exoplanetary systems (Haywood et al. 2014), also within the HADES collaboration (Affer et al. 2016; Perger et al. 2017b; Pinamonti et al. 2018). We have used a quasi-periodic kernel to model the correlated RV signal due to stellar activity, and we refer to one of the previous papers for the details about the quasi-periodic model. Here we summarize the meaning of the GP hyper-parameters included in the quasi-periodic kernel, as discussed in this work:  $h$  is the amplitude of the correlations (we consider two  $h$  parameters, one in common for HARPS and HARPS-N and one for HIRES, on account of possible differences related to the use of different instruments);  $\theta$  is the recurrence time of the correlations (generally, the stellar rotation period); the parameter  $w$  describes the level of high-frequency variation within a single stellar rotation, and it is related to the distribution of the features on the stellar surface related to the magnetic activity; and  $\lambda$  is the correlation decay time scale, that can be physically related to the lifetime of the magnetically active regions.

The use of the quasi-periodic GP regression in our work seems justified after the analysis previously described, which showed that signals modulated at the stellar rotation have been

identified in ancillary data and could be also present in the RV dataset. We have first fitted the RVs without including a Keplerian in the model, which then represents the 'null scenario' against which to compare the model with one planet within a Bayesian framework. We have performed the Monte Carlo sampling within a Gaussian process framework using the open source Bayesian inference tool `MultiNestv3.10` (e.g. Feroz et al. 2013), through the python wrapper `pyMultiNest` (Buchner et al. 2014), with 800 live points and a sampling efficiency of 0.3. We have integrated into our code the publicly available GP module `GEORGEv0.2.1` (Ambikasaran et al. 2014). Table 4 summarizes the best-fit values for the (hyper-)parameters of the one planet circular model, which includes RV offsets and uncorrelated jitter terms for each instrument. It is very strongly favored over the 'null scenario' and even more over the one-planet eccentric model, according to the Bayesian evidence ( $\ln \mathcal{Z}$ ) calculated by `MultiNest` ( $\Delta \ln \mathcal{Z} = \ln \mathcal{Z}_{1\text{-plan, circ}} - \ln \mathcal{Z}_{\text{othermodel}} = 22$  and 25, respectively). In all the cases we have used a large uninformative prior on the hyper-parameter  $\theta$ , and the posterior for the case of the one-planet model is quasi symmetric and narrowly centered around  $\sim 37$  days. This result is in very good agreement with the expected stellar rotation period, as derived from the analysis of ancillary data. As a consequence of our choice of quite unconstrained priors for the stellar activity term, the hyper-parameter  $\lambda$  shows a bi-modal posterior, with the maximum a posteriori (MAP) value of  $\sim 44$  days. The first mode with the higher values corresponds to samples with higher  $\theta$ : in fact, by selecting only samples for which  $\lambda > 16$  days, we get  $\theta = 38_{-2}^{+4}$  days. This is what has to be expected, since a higher evolutionary time scale of the active regions should imply a more precise determination of the stellar rotation period. However, we note that the planetary parameters are not affected by the particular representation of the stellar activity term. Our unconstrained GP analysis shows that a signal modulated on the expected stellar rotation period is indeed present in the data. In Fig. 8 we show the marginal posterior distributions for the parameters of our model, one planet on a circular orbit + stellar activity.

We tested the nature of the 15.5-day signal by applying the apodized Keplerian model proposed by Gregory (2016), in which the semi-amplitude  $K$  of the planetary orbital equation is multiplied by a symmetrical Gaussian of unknown width  $\tau$  and with an unknown centre of the apodizing window  $t_a$ . We get clear evidence that  $\tau$  converges toward values much higher than the time span of the data ( $\tau = 20278_{-8250}^{+7827}$  days, with prior  $\mathcal{U}(1, 32000)$ ), indicating that  $K$  is constant over the range of the observations.

As a second test on the nature of the 15.5 d signal, we performed a GP + 1 Keplerian planetary signal model, using three different inferior conjunction times ( $T_0$ ), one for each season described in Sec. 3.4, but leaving the set-up of the general parameters substantially unmodified. Each  $T_0$  has been searched around a value close to the center of each observing season, in order to obtain similar uncertainties for each of them. Using the best-fit orbital period, the  $T_0$  posterior distribution has been scaled to a single value, obtaining as a result [BJD-2450000]:

- $T_{01} = 5615.15_{-0.46}^{+0.48}$  days
- $T_{02} = 5615.4 \pm 0.36$  days
- $T_{03} = 5616.31_{-0.33}^{+0.35}$  days

The  $T_0$  values of the first two seasons are well within the errors ( $0.55 \sigma$ ), while  $T_{03}$  is  $1.6 \sigma$  from  $T_{02}$ . Therefore, these two tests support the planetary interpretation of the RV signal.

We used the results of the one-planet circular model to verify if the planetary signal has a significant eccentricity by imposing

a narrow uniform prior on  $\theta$  ( $\mathcal{U}(34, 42)$  days) and a larger prior on  $P_b$  ( $\mathcal{U}(0, 20)$  days). We recover a solution which is very similar to that for the circular case, where the eccentricity is compatible with zero ( $e = 0.05_{-0.03}^{+0.05}$ ). Fig. 9 shows the RV curve folded at the best-fit orbital period for the detected planet. In Fig. 10 we show the RV residuals, after the Keplerian has been removed, with superposed the best fit stellar correlated, quasi-periodic signal.

We also tested a model involving two Keplerian signals which, as expected from our previous analyses, appears less probable than that with one planet ( $\ln \mathcal{Z} = -510.63 \pm 0.27$ ). With this model we always obtain the stellar rotation period, as before, and it is worth noticing that the parameters of the planet Gl 686 b remain almost unchanged in the transition from models with a different number of planets.

### 5.1. Bayesian analysis of the $H\alpha$ time series

We performed the Bayesian analysis of the  $H\alpha$  index, obtained from the HARPS and HARPS-N spectra, corrected for instrumental offset. We used the same prior as in the case of RV analysis (see Table 5).

The  $H\alpha$  analysis indicates that the distribution obtained for  $\theta$  is bimodal (1 year alias) and the first peak is around 37 d, that is the same result we obtained in the planetary case. The  $\lambda$  value is larger than that obtained considering the RVs time series, though the two datasets are not comparable ( $H\alpha$  data are only from the two HARPS instruments), both in terms of time span and number of data points.

## 6. DISCUSSION

Several works on M stars (e.g., Kürster et al. 2003; Robertson et al. 2014, 2015), have highlighted that the activity signals that create RV shifts, might not create a detectable photometric periodicity. This can happen in several cases, when magnetic phenomena inhibit the convection but do not create dark spots on the surface of the star, thereby altering RVs without a corresponding photometric signature. Actually, we observed this phenomenon also for Gl 686, for which the ancillary photometric observations, but for ASAS photometry, do not detect a clear periodicity.

We can speculate about the physical meaning of the recurrent period at 45 d (both in RV and activity time series), ascribing it to differential rotation, i.e. latitudinal differences in the rotation velocity. In general, differential rotation is not yet fully understood, as is discussed in Küker & Rüdiger (2011). In their work on solar-type stars, Reiners & Schmitt (2003) considered a calibration of the ratio between the positions of the two first zeros of the power spectrum of the line profile (in the Fourier domain) as a function of the ratio  $\alpha$  between equatorial and polar rotation rate. They obtained an anticorrelation between differential rotation and equatorial velocity: differential rotation is mostly evident in slow rotators, like Gl 686. However, Reiners & Schmitt only considered solar-type stars and did not show that we might see such trends in time series of M dwarfs. Reinhold & Gizon (2015) analyzed an extremely wide dataset of stars, observed with Kepler, ranging from solar-type stars to M dwarfs and confirmed the relation found by Reiners & Schmitt between differential rotation and period. We may directly compare our result for Gl 686 with Fig. 9 of Reinhold & Gizon, where they plotted the minimum rotation period (in our case 37 d), with the parameter  $\alpha = (P_{\text{max}} - P_{\text{min}}) / P_{\text{max}}$ . For Gl 686,  $\alpha = (45 - 37) / 45 = 0.177$ .

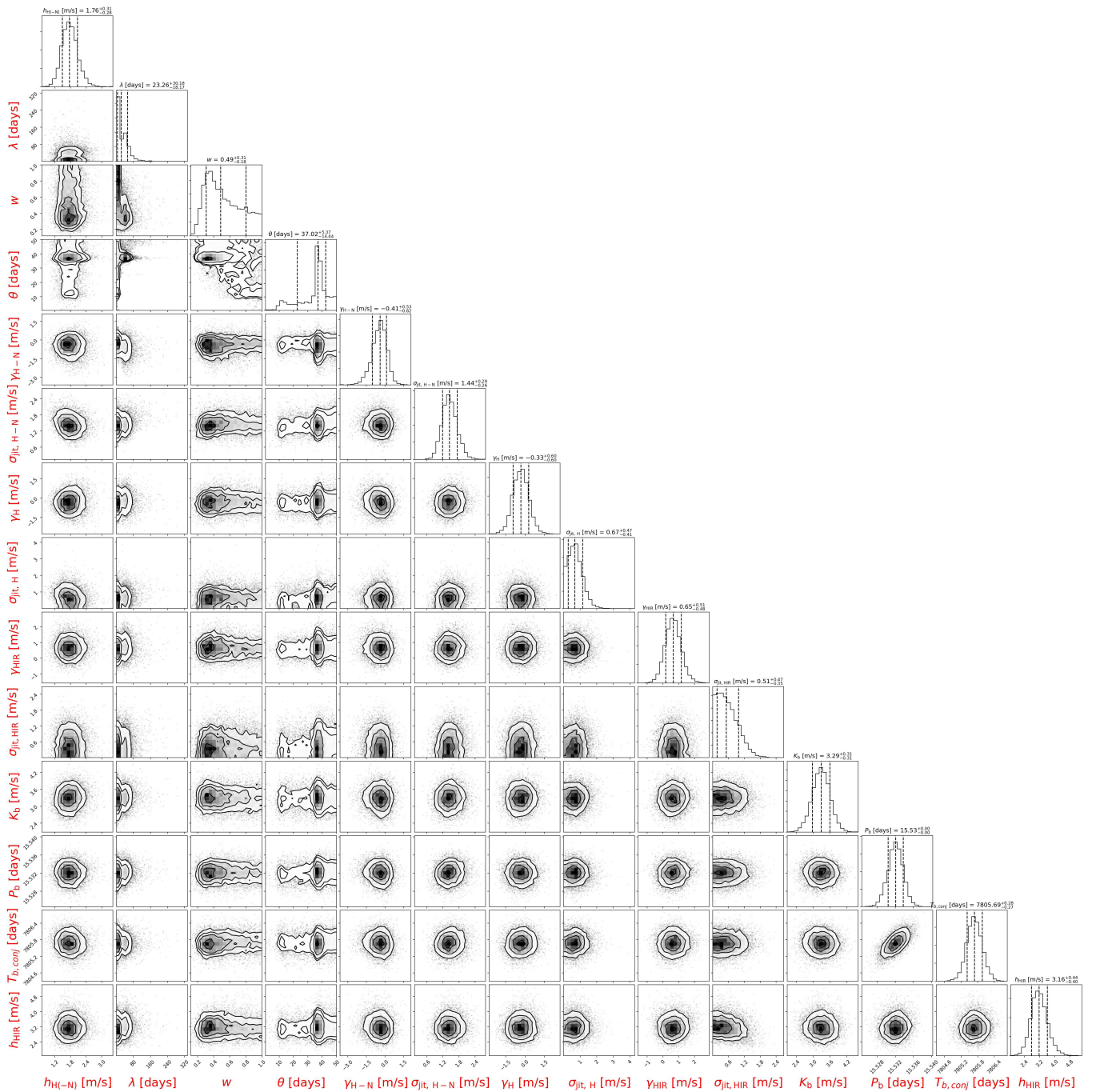


**Fig. 8.** Marginal posterior distributions for the parameters of our model, which includes one Keplerian, for the RV data. H stands for HARPS, H-N for HARPS-N, and HIR for HIRES, in the labels.

The point for G1 686 falls exactly in the middle of the points for the M stars. We conclude that the assumption that this two periods related to activity for G1 686 are due to rotation is fully consistent with what we know about differential rotation. Looking at the *Gaia* solution, it appears that the residues in the astrometric solution are small and there is no evidence of significant noise. This point, coupled with the fact that there is no trend in radial velocity, suggests that there are no giant planets in the system, even at separations of some astronomical units. Moreover, *Gaia* did not find any companion within a degree; this also places limits on massive brown dwarfs with great separation (a result that depends on age, unknown for G1 686). The results within the HADES survey so far, confirm that the fre-

quency of giant companions around M stars is lower than the one around solar-type hosts, a result that is now rather well observationally established, as clearly shown in Endl et al. (2006) (see also, Sozzetti et al. 2014; Dressing & Charbonneau 2015, and references therein).

The main interest in focusing the research of extrasolar planets around M stars is to discover an Earth twin, a planet lying in the HZ of the system star-planet. However, the topic is very complex and, apart from the star-planet separation and stellar luminosity, many other factors also influence habitability like the planetary environment e.g. planet albedo, composition, and the amount of greenhouse gases in the atmosphere (Kaltenegger et al. 2010). Moreover, planets in close orbits around low mass stars are prob-

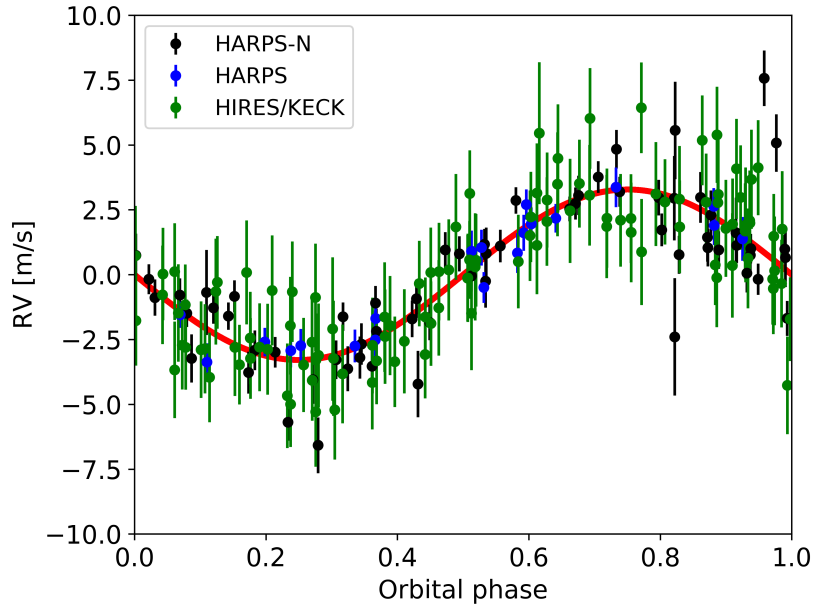


**Fig. 9.** RV data folded at the best-fit orbital period of the planet. The red solid line is the best-fit orbital solution.

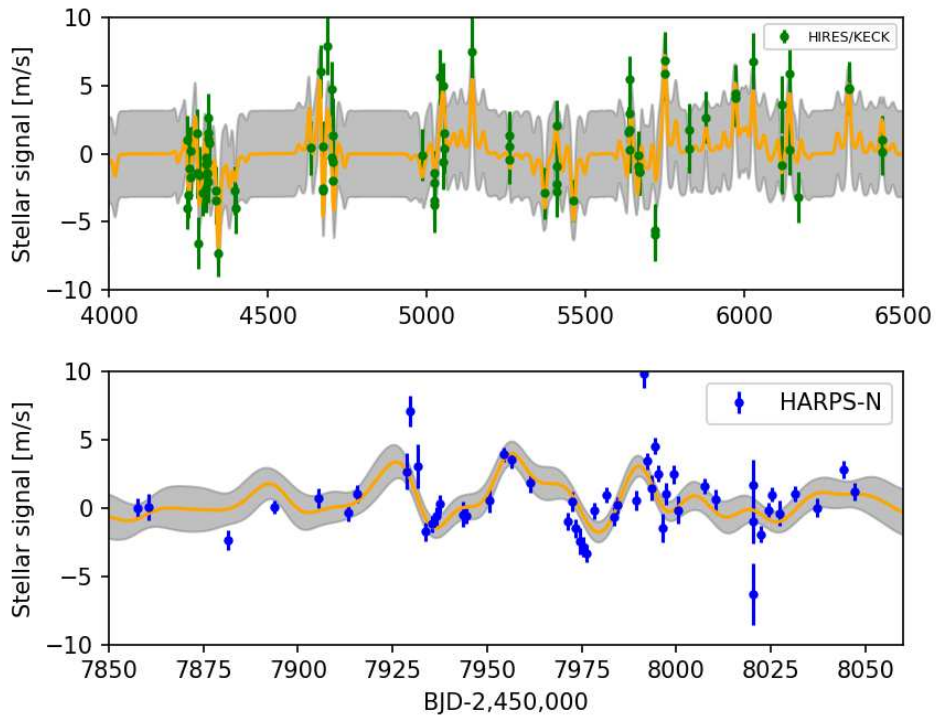


**Fig. 10.** Blow-up of the best-fit quasi-periodic signal of two particularly crowded regions (orange line) for HIRES data (upper panel) and HARPS-N (lower panel), the grey areas mark the uncertainties band  $\pm 1\sigma$ .

**Table 5.** Best fit values for the hyper parameters of the covariance function, derived from a GP analysis of the  $H\alpha$  activity index time series.

Parameter	Value	Prior
$h$	$0.01061^{+0.00255}_{-0.00192}$	$\mathcal{U}(0,20)$
$\lambda$ [days]	$251^{+152}_{-126}$	$\mathcal{U}(0,8000)$
$w$	$0.872^{+0.091}_{-0.149}$	$\mathcal{U}(0,1)$
$\theta$ [days]	$39.38^{+2.32}_{-2.28}$	$\mathcal{U}(0,50)$

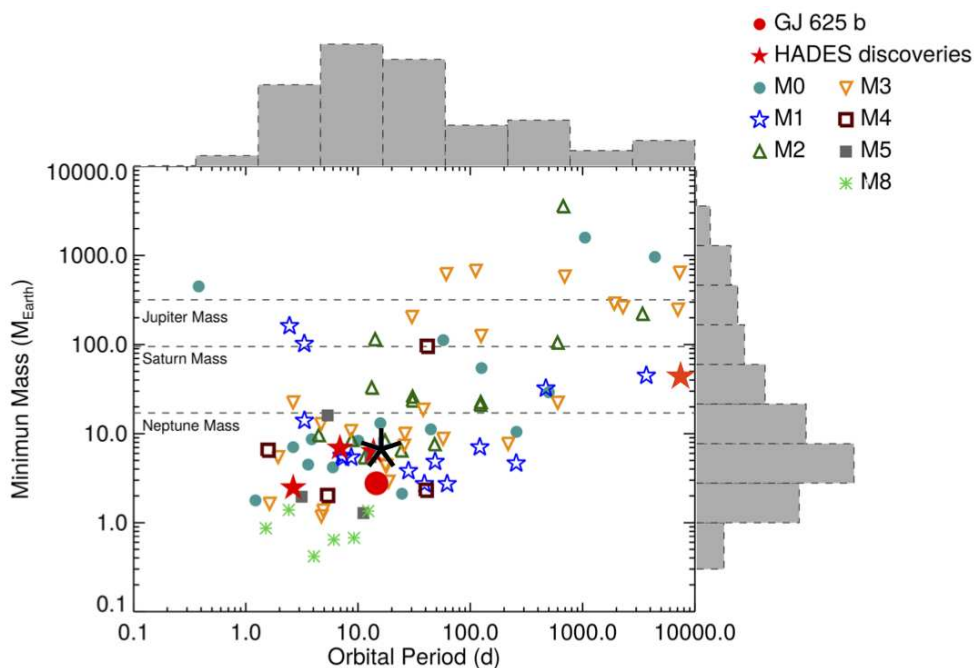


**Fig. 11.** Adaptation of Fig. 21 from Suárez Mascareño et al. (2017), showing minimum mass vs. orbital period for the known planets with determined masses around M-dwarf stars (using exoplanet.eu data) divided by the spectral type of the host star. The red filled stars show the positions of HADES planets, the red filled dot shows the position of the planet GJ 625 b, the black asterisk has been added to show the position of GJ 625 b. The horizontal dashed lines show the mass of the solar system planets for comparison. The distribution for each parameter is shown at the edges of the figure.

ably tidally locked, thus only one side of the planet is strongly irradiated by the star and the possible redistribution of the incident energy on both hemispheres is strictly subjected to the existence of an atmosphere, to its composition and circulation. The equilibrium temperature of the planet is derived using the Stefan-Boltzmann law (ignoring the greenhouse effect):

$$T_{eq} = T_{\star} \left( \frac{R_{\star}}{2a} \right)^{1/2} [f(1 - A_B)]^{1/4},$$

where  $T_{\star}$  is the stellar effective temperature and  $a$  is the semi-major axis of the planet.  $A_B$  is the Bond albedo and the  $f$  factor describes the atmospheric circulation. If the planet is tidally locked to its star, but advection distributes the incident energy over both hemispheres, we can assume  $f = 1$ . If only the dayside reradiates the incident energy, the higher equilibrium temperature is given by  $f = 2$  (e.g., Charbonneau et al. 2005; Méndez & Rivera-Valentín 2017). Thus, we can derive an upper limit on  $T_{eq}$  by setting  $A_B = 0$ . In the two extreme cases,  $f = 1$  and  $f = 2$ , for GJ 625 b  $T_{eq} = 379$  K and 450 K, respectively.

We estimated the conservative inner limits of the habitable zone for GJ 625 b, following Kasting et al. (1993) and Kopparapu et al. (2013). The optimistic inner limit (*recent Venus*) corresponds to a semi-major axis of 0.137 AU, for the HZ of GJ 625 b. To estimate a more optimistic inner limit, we followed the empirical fitting formulas of Zsom et al. (2013), which provide a inner edge limit of 0.1 AU, for a surface albedo of 0.2 and 1% relative humidity, and a limit of 0.07 AU, for a surface albedo of 0.8. Thus, we tentatively can state that GJ 625 b could be located inside, or near the inner limit of the HZ, depending on its atmospheric conditions.

## 7. SUMMARY AND CONCLUSION

For the star GJ 625 b, we took advantage of our own observing campaign, within the HADES programme with HARPS-N, and of public archive data, obtained with HARPS and HIRES. The composite dataset covers a timespan of more than 20 years. The very wide coverage of RV data and the persistence of the signal in such a long timespan, make GJ 625 b an interesting target not only for planet detection purposes but, particularly, for the study of the behavior of activity in M dwarfs.

We detected one significant radial velocity signal at a period of 15.53 d, both in each one of the datasets and in the composite time series. The dominant periodicity shows a very high spectral power. In order to shed a light on the real origin of the signal we performed a complete analysis of the RV and activity indexes time series as well as the study of photometric light-curve, using the Gaussian processes amongst other techniques. The periods related to activity effects span a range from 27 to 45 d, and the significant peaks in the GLS of several activity indicators (related to magnetic phenomena such as spots and faculae, which rotate on the stellar surface, and to differential rotation), are not stable during the seasons/datasets (37, 38, 40 and 45 d in the three seasons/telescope datasets). The second radial velocity signal of period 36.7 d in HARPS-N data, also suggested by several activity indicators ( $H\alpha$  37.05 d in HARPS-N data and  $S$ -index 38 d in HIRES data) and by the Gaussian Process (37 d) and ASAS photometry (37.8 d), provide an estimate of the rotation period and also of the variability of the spots configuration during the long timespan, and the hint of an activity cycle  $\sim 2000$  d long. Conversely, the spectral feature at 15.53 d is a coherent signal, observed to stay stable during all the three seasons.

We used a Bayesian model selection to determine the probability of the existence of a planet in the system and estimate the orbital

parameters and minimum mass. We tested several different models in which we varied the number of planets (0, 1, 2) and the eccentricity, varying the prior ranges. We selected a model involving one Keplerian circular signal and a GP describing stellar activity variations (the two Keplerian + GP model has a lower Bayesian evidence).

From the available photometric and spectroscopic information we conclude that the 15.53 d signal is caused by a planet with a minimum mass of  $7.1 \pm 0.9 M_{\oplus}$ , in an orbit with a semi-major axis of 0.09 AU.

Gl 686 b goes to populate the lower part of the diagram of minimum mass vs orbital period of the known planets around M stars, as well as the other super-Earths discovered within the HADES programme, GJ 3998 b and GJ 3998 c (Affer et al. 2016), GJ 625 b (Suárez Mascareño et al. 2017) and GJ 3942 b (Perger et al. 2017b) (see Fig. 11, adapted from Suárez Mascareño et al. 2017).

Following the preliminary results of the HADES survey, one characteristic of the behaviour of M dwarfs planetary systems, that seems to emerge, is the recurrency of planetary systems having planet minimum mass lower than  $10 M_{\oplus}$ , with orbital periods in the range 10-20 d and stellar rotation periods between 30 and 40 d.

*Acknowledgements.* GAPS acknowledges support from INAF through the Progetti Premiali funding scheme of the Italian Ministry of Education, University, and Research. LA, GM, JM, AG and MD acknowledge financial support from Progetto Premiale 2015 FRONTIERA (OB.FU. 1.05.06.11) funding scheme of the Italian Ministry of Education, University, and Research. GS acknowledges financial support from “Accordo ASI-INAF” No. 2013-016-R.0 July 9, 2013 and July 9, 2015. MP, and IR, acknowledge support from the Spanish Ministry of Economy and Competitiveness (MINECO) and the Fondo Europeo de Desarrollo Regional (FEDER) through grant ESP2016-80435-C2-1-R, as well as the support of the Generalitat de Catalunya/CERCA program. JIGH, RR and BTP acknowledge financial support from the Spanish Ministry project MINECO AYA2017-86389-P, and JIGH from the Spanish MINECO under the 2013 Ramón y Cajal programme MINECO RYC-2013-14875. MP gratefully acknowledges the support from the European Union Seventh Framework Programme (FP7/2007-2013) under Grant Agreement No. 313014 (ETA-EARTH).

This work is based on observations made with the Italian Telescopio Nazionale Galileo (TNG), operated on the island of La Palma by the Fundación Galileo Galilei of the Istituto Nazionale di Astrofisica (INAF) at the Spanish Observatorio del Roque de los Muchachos (ORM) of the Instituto de Astrofísica de Canarias (IAC).

We wish to thank the anonymous referee for thoughtful comments and suggestions that helped improve the manuscript.

## References

Affer, L., Micela, G., Damasso, M., et al. 2016, *A&A*, 593, A117  
 Ambikasaran, S., Foreman-Mackey, D., Greengard, L., Hogg, D. W., & O’Neil, M. 2014  
 Anglada-Escudé, G., Amado, P. J., Barnes, J., et al. 2016, *Nature*, 536, 437  
 Anglada-Escudé, G. & Butler, R. P. 2012, *ApJS*, 200, 15  
 Astudillo-Defru, N., Bonfils, X., Delfosse, X., et al. 2015, *A&A*, 575, A119  
 Astudillo-Defru, N., Delfosse, X., Bonfils, X., et al. 2017a, *A&A*, 600, A13  
 Astudillo-Defru, N., Díaz, R. F., Bonfils, X., et al. 2017b, *A&A*, 605, L11  
 Bensby, T., Feltzing, S., & Lundström, I. 2004, *A&A*, 421, 969  
 Bonfils, X., Delfosse, X., Udry, S., et al. 2013, *A&A*, 549, A109  
 Box, G. E. P. & Jenkins, G. M., eds. 1976, *Time series analysis. Forecasting and control*  
 Buchner, J., Georgakakis, A., Nandra, K., anad Hsu, L., et al. 2014, *A&A*, 564, A125  
 Butler, R. P., Vogt, S. S., Laughlin, G., et al. 2017, *AJ*, 153, 208  
 Charbonneau, D., Allen, L. E., Megeath, S. T., et al. 2005, *ApJ*, 626, 523  
 Charbonneau, D. & Deming, D. 2007, *ArXiv e-prints* [arXiv:0706.1047]  
 Cosentino, R., Lovis, C., Pepe, F., et al. 2012, in *Proc. SPIE*, Vol. 8446, Ground-based and Airborne Instrumentation for Astronomy IV, 84461V  
 Crossfield, I. J. M., Petigura, E., Schlieder, J. E., et al. 2015, *ApJ*, 804, 10  
 Cutri, R. M., Skrutskie, M. F., van Dyk, S., et al. 2003, *VizieR Online Data Catalog*, 2246  
 Dawson, R. I. & Fabrycky, D. C. 2010, *ApJ*, 722, 937

Delfosse, X., Bonfils, X., Forveille, T., et al. 2013, *A&A*, 553, A8  
 Dressing, C. D. & Charbonneau, D. 2015, *ApJ*, 807, 45  
 Edelson, R. A. & Krolik, J. H. 1988, *ApJ*, 333, 646  
 Endl, M., Cochran, W. D., Kürster, M., et al. 2006, *ApJ*, 649, 436  
 Endl, M., Kürster, M., Els, S., Hatzes, A. P., & Cochran, W. D. 2001, *A&A*, 374, 675  
 Feroz, F., Hobson, M. P., Cameron, E., & Pettitt, A. N. 2013, *ArXiv e-prints* [arXiv:1306.2144]  
 Forveille, T., Bonfils, X., Delfosse, X., et al. 2009, *A&A*, 493, 645  
 Gaia Collaboration. 2018, *VizieR Online Data Catalog*, 1345  
 Gaia Collaboration, Prusti, T., de Bruijne, J. H. J., et al. 2016, *A&A*, 595, A1  
 Gaidos, E. 2013, *ApJ*, 770, 90  
 Giampapa, M. S., Cram, L. E., & Wild, W. J. 1989, *ApJ*, 345, 536  
 Gillon, M., Triaud, A. H. M. J., Demory, B.-O., et al. 2017, *Nature*, 542, 456  
 Gregory, P. C. 2016, *MNRAS*, 458, 2604  
 Haywood, R. D., Collier Cameron, A., Queloz, D., et al. 2014, *MNRAS*, 443, 2517  
 Howard, A. W., Marcy, G. W., Fischer, D. A., et al. 2014, *ApJ*, 794, 51  
 Kaltenegger, L., Eiroa, C., Ribas, I., et al. 2010, *Astrobiology*, 10, 103  
 Kass, R. E. & Raftery, A. E. 1995, *Journal of the American Statistical Association*, 90, 773  
 Kasting, J. F., Whitmire, D. P., & Reynolds, R. T. 1993, *Icarus*, 101, 108  
 Koen, C., Kilkenny, D., van Wyk, F., & Marang, F. 2010, *MNRAS*, 403, 1949  
 Kopparapu, R. K., Ramirez, R., Kasting, J. F., et al. 2013, *ApJ*, 765, 131  
 Küker, M. & Rüdiger, G. 2011, *Astronomische Nachrichten*, 332, 933  
 Kürster, M., Endl, M., Rouesnel, F., et al. 2003, *A&A*, 403, 1077  
 Lenz, P. & Breger, M. 2004, in *IAU Symposium*, Vol. 224, The A-Star Puzzle, ed. J. Zverko, J. Ziznovsky, S. J. Adelman, & W. W. Weiss, 786–790  
 Lovis, C., Dumusque, X., Santos, N. C., et al. 2011, *ArXiv e-prints* [arXiv:1107.5325]  
 Lovis, C. & Pepe, F. 2007, *A&A*, 468, 1115  
 Maldonado, J., Affer, L., Micela, G., et al. 2015, *A&A*, 577, A132  
 Maldonado, J., Scandariato, G., Stelzer, B., et al. 2017, *A&A*, 598, A27  
 Mandell, A. M., Raymond, S. N., & Sigurdsson, S. 2007, *ApJ*, 660, 823  
 Mayor, M., Pepe, F., Queloz, D., et al. 2003, *The Messenger*, 114, 20  
 Méndez, A. & Rivera-Valentín, E. G. 2017, *ApJ*, 837, L1  
 Mortier, A. & Collier Cameron, A. 2017, *A&A*, 601, A110  
 Perger, M., García-Piquer, A., Ribas, I., et al. 2017a, *A&A*, 598, A26  
 Perger, M., Ribas, I., Damasso, M., et al. 2017b, *A&A*, 608, A63  
 Pinamonti, M., Damasso, M., Marzari, F., et al. 2018, *A&A*, 617, A104  
 Pojmanski, G. 1997, *Acta Astron.*, 47, 467  
 Reiners, A. & Schmitt, J. H. M. M. 2003, *A&A*, 398, 647  
 Reinhold, T. & Gizon, L. 2015, *A&A*, 583, A65  
 Ribas, I., Tuomi, M., Reiners, A., et al. 2018, *Nature*, 563, 365  
 Robertson, P., Mahadevan, S., Endl, M., & Roy, A. 2014, *Science*, 345, 440  
 Robertson, P., Roy, A., & Mahadevan, S. 2015, *ApJ*, 805, L22  
 Scandariato, G., Maldonado, J., Affer, L., et al. 2017, *A&A*, 598, A28  
 Sozzetti, A., Bernagozzi, A., Bertolini, E., et al. 2013, in *European Physical Journal Web of Conferences*, Vol. 47, *European Physical Journal Web of Conferences*, 03006  
 Sozzetti, A., Giacobbe, P., Lattanzi, M. G., et al. 2014, *MNRAS*, 437, 497  
 Suárez Mascareño, A., González Hernández, J. I., Rebolo, R., et al. 2017, *A&A*, 605, A92  
 Suárez Mascareño, A., Rebolo, R., González Hernández, J. I., et al. 2018, *A&A*, 612, A89  
 Tal-Or, L., Trifonov, T., Zucker, S., Mazeh, T., & Zechmeister, M. 2018, *ArXiv e-prints* [arXiv:1810.02986]  
 Tuomi, M., Jones, H. R. A., Barnes, J. R., Anglada-Escudé, G., & Jenkins, J. S. 2014, *MNRAS*, 441, 1545  
 Vaníček, P. 1971, *Ap&SS*, 12, 10  
 Wright, J. T. & Howard, A. W. 2009, *ApJS*, 182, 205  
 Zechmeister, M. & Kürster, M. 2009, *A&A*, 496, 577  
 Zsom, A., Seager, S., de Wit, J., & Stamenković, V. 2013, *ApJ*, 778, 109

## Appendix A: Appendix

In this section we report the observational data collected with the HARPS-N and HARPS spectrographs (from TERRA pipeline), the uncertainties are the internal errors; the time series plots of the activity indexes (*S*-index,  $H\alpha$ , NaD); the time series plots of the ASAS and EXORAP photometry; the phase folded plots, at the most significant periods of the GLS analysis of activity indexes.

**Table A.1.** RV time series from HARPS and HARPS-N.

BJD (d)	RV (m s <sup>-1</sup> )	dRV (m s <sup>-1</sup> )	Instrument
2453159.74925	3.622	0.708	HARPS
2453574.62253	0.683	0.694	HARPS
2453817.86816	-1.087	0.640	HARPS
2454174.87132	-1.876	0.646	HARPS
2454194.90763	2.401	0.691	HARPS
2454300.64483	-2.806	0.631	HARPS
2454948.86153	-1.510	0.506	HARPS
2454950.86206	-2.799	0.545	HARPS
2454956.83070	-0.860	0.770	HARPS
2455390.64094	0.913	0.793	HARPS
2455392.63268	1.920	0.551	HARPS
2455407.58589	0.750	0.630	HARPS
2455409.58801	2.104	0.765	HARPS
2455412.57851	0.209	0.845	HARPS
2455437.52933	-3.101	0.592	HARPS
2455438.53350	0.0	0.583	HARPS
2455446.52185	-6.482	0.725	HARPS
2455450.49607	-4.481	1.137	HARPS
2455450.50812	-3.653	0.795	HARPS
2455458.50534	0.540	0.750	HARPS
2456700.74950	3.449	0.976	HARPS-N
2456702.75851	1.131	1.143	HARPS-N
2457508.59296	-0.499	0.720	HARPS-N
2457510.60844	-0.557	0.841	HARPS-N
2457536.60127	0.890	0.755	HARPS-N
2457537.57229	0.927	0.576	HARPS-N
2457538.56821	-0.596	0.630	HARPS-N
2457606.46289	-7.009	0.809	HARPS-N
2457608.52949	-6.822	0.744	HARPS-N
2457609.48134	-5.751	0.881	HARPS-N
2457610.46819	-7.729	1.278	HARPS-N
2457857.64182	-3.148	0.800	HARPS-N
2457860.58996	0.398	1.000	HARPS-N
2457881.61942	-0.658	0.725	HARPS-N
2457893.62668	2.509	0.480	HARPS-N
2457905.54171	-1.052	0.734	HARPS-N
2457913.42783	0.568	0.659	HARPS-N
2457915.48199	-0.733	0.643	HARPS-N
2457928.62545	3.966	1.357	HARPS-N
2457929.57855	7.202	1.111	HARPS-N
2457931.64334	0.590	1.638	HARPS-N
2457933.57005	-5.395	0.713	HARPS-N
2457935.55273	-4.075	0.632	HARPS-N
2457936.50234	-2.522	0.708	HARPS-N
2457937.61603	-0.228	0.677	HARPS-N
2457943.56272	1.447	0.943	HARPS-N
2457944.50282	0.271	0.568	HARPS-N
2457950.51349	-2.784	0.864	HARPS-N
2457954.48680	5.138	0.510	HARPS-N
2457956.43367	6.301	0.611	HARPS-N
2457961.48733	0.790	0.701	HARPS-N
2457971.42438	1.530	0.621	HARPS-N
2457972.39543	3.350	0.744	HARPS-N
2457973.39354	1.255	0.687	HARPS-N
2457974.54434	-0.441	0.942	HARPS-N
2457975.47540	-1.869	0.741	HARPS-N
2457976.42985	-3.568	0.670	HARPS-N
2457978.40128	-2.844	0.608	HARPS-N
2457981.46533	-2.406	0.545	HARPS-N
2457983.51089	-2.040	0.686	HARPS-N

**Table A.1.** continued.

BJD (d)	RV (m s <sup>-1</sup> )	dRV (m s <sup>-1</sup> )	Instrument
2457984.49862	0.076	0.592	HARPS-N
2457989.40811	3.048	0.732	HARPS-N
2457991.41740	10.348	1.070	HARPS-N
2457992.41040	2.595	0.575	HARPS-N
2457993.41983	-0.627	0.927	HARPS-N
2457994.43299	1.466	0.616	HARPS-N
2457995.39168	-1.058	0.592	HARPS-N
2457996.40619	-5.063	1.074	HARPS-N
2457997.39394	-2.061	0.814	HARPS-N
2457999.41286	1.526	0.688	HARPS-N
2458000.36403	0.180	1.018	HARPS-N
2458007.43803	1.455	0.547	HARPS-N
2458010.44627	-2.780	0.767	HARPS-N
2458020.35765	1.627	1.628	HARPS-N
2458020.36872	-3.716	2.265	HARPS-N
2458020.37951	4.244	1.877	HARPS-N
2458022.34095	-1.270	0.603	HARPS-N
2458024.36957	-2.123	0.528	HARPS-N
2458025.35424	-1.982	0.528	HARPS-N
2458027.34820	-4.022	0.935	HARPS-N
2458031.40518	1.328	0.593	HARPS-N
2458037.36400	1.270	0.675	HARPS-N
2458044.36215	0.0	0.665	HARPS-N
2458047.31078	1.944	0.626	HARPS-N

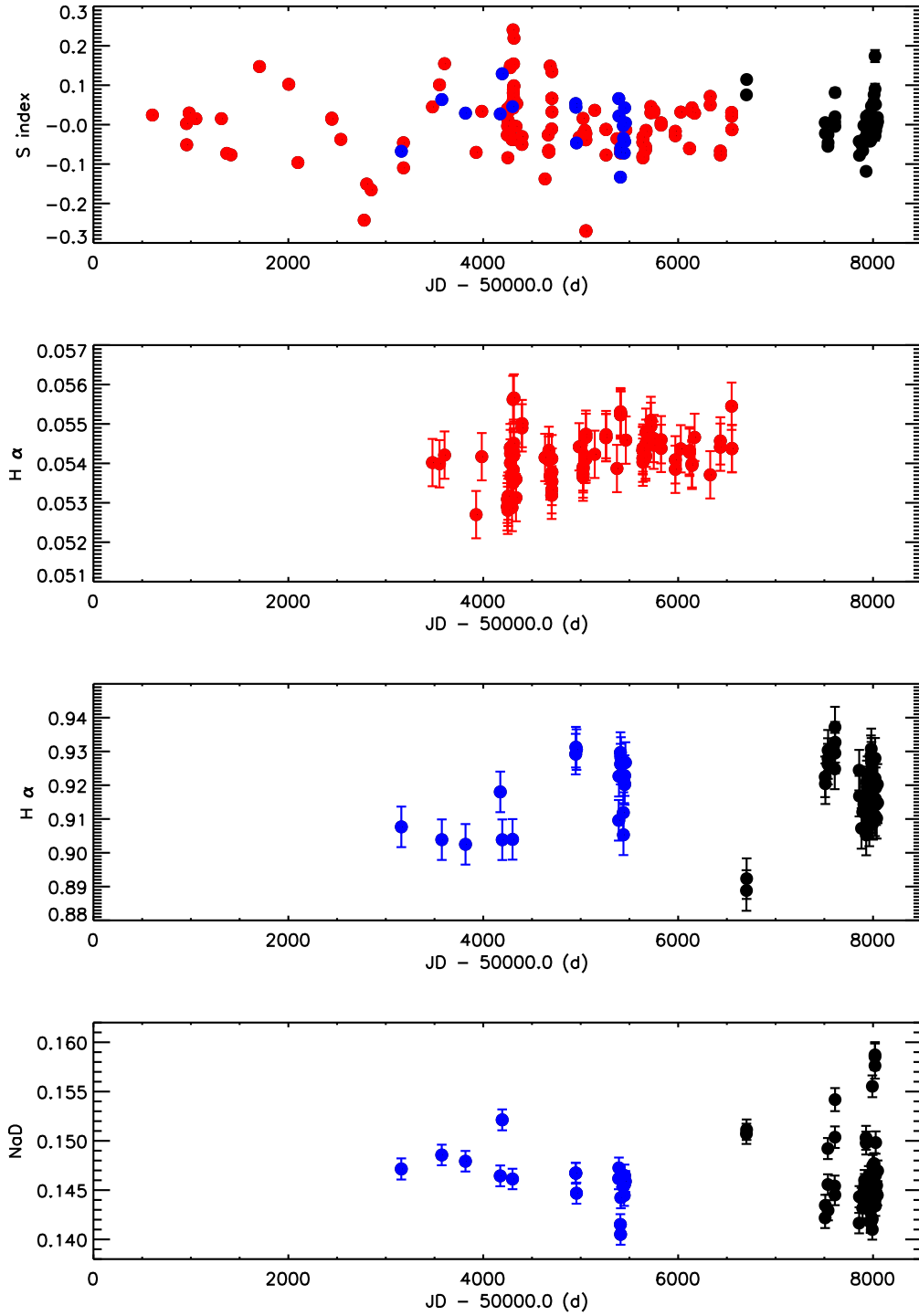


**Fig. A.1.** Time series data of the activity indexes,  $S$ -index (HIRES/red, HARPS/blue, HARPS-N/black),  $H\alpha$  (HIRES/red),  $H\alpha$ , and NaD (HARPS/blue, HARPS-N/black), from top to bottom.

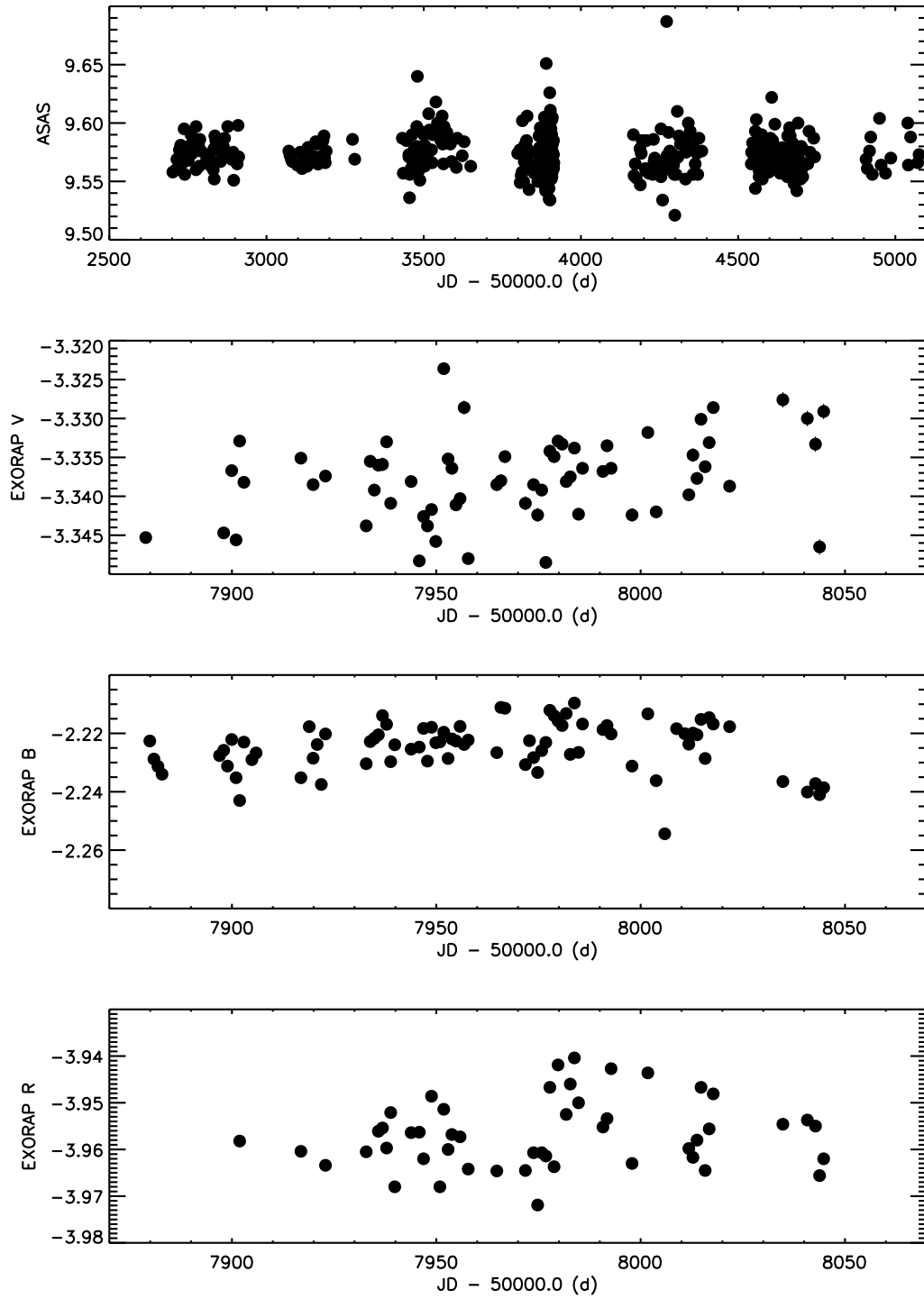


**Fig. A.2.** Photometric time series: ASAS, EXORAP V, EXORAP B, EXORAP R, from top to bottom. The y axis indicates flux for ASAS data, differential magnitudes for EXORAP data.

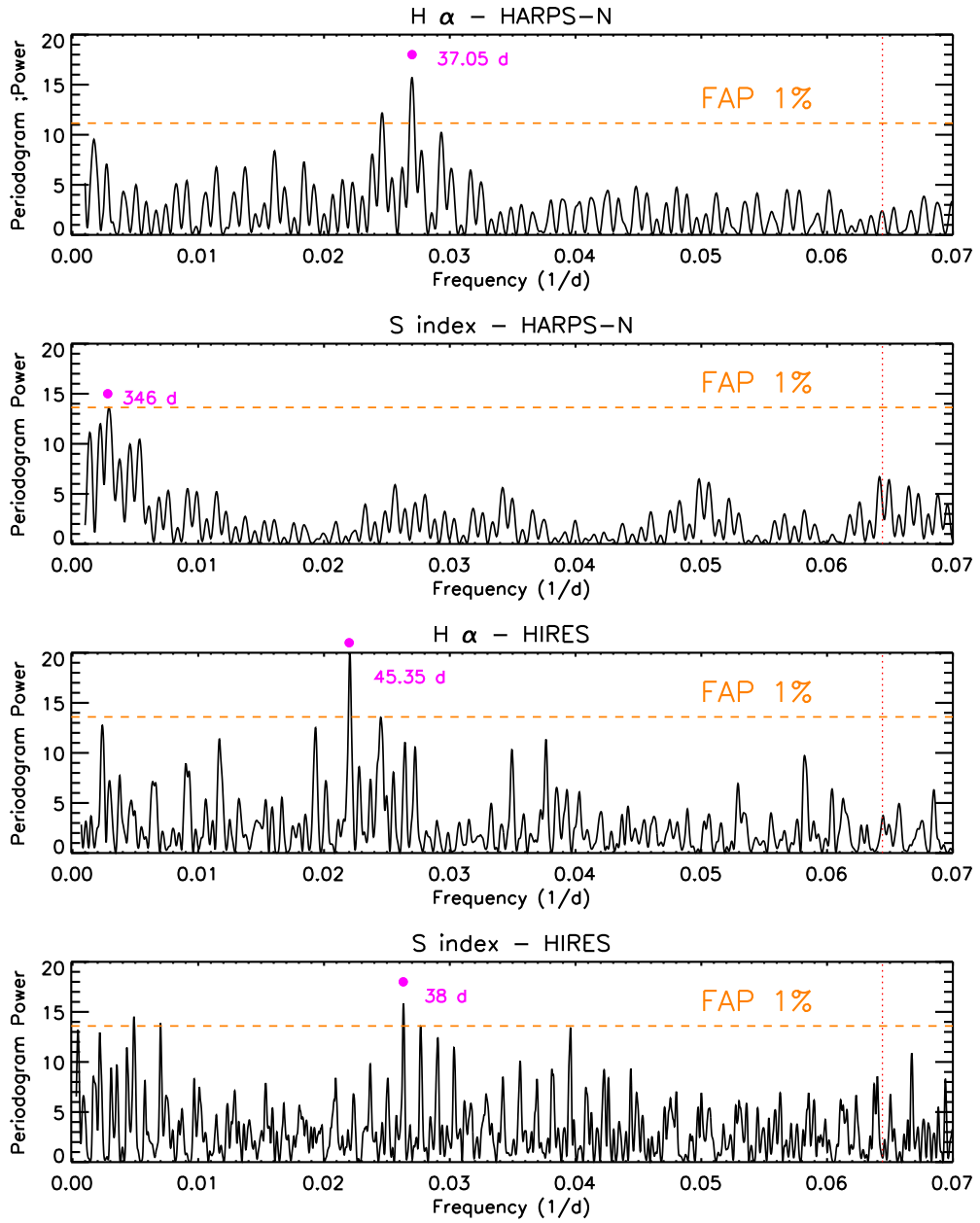


**Fig. A.3.** GLS periodograms of activity indexes (from top to bottom):  $H\alpha$  and Sindex (HARPS-N);  $H\alpha$  and Sindex (HIRES). The 15.5 d period is indicated in each periodogram, as the red dashed line. The significant periods discussed in Sect. 3.4, are indicated with a magenta dot.

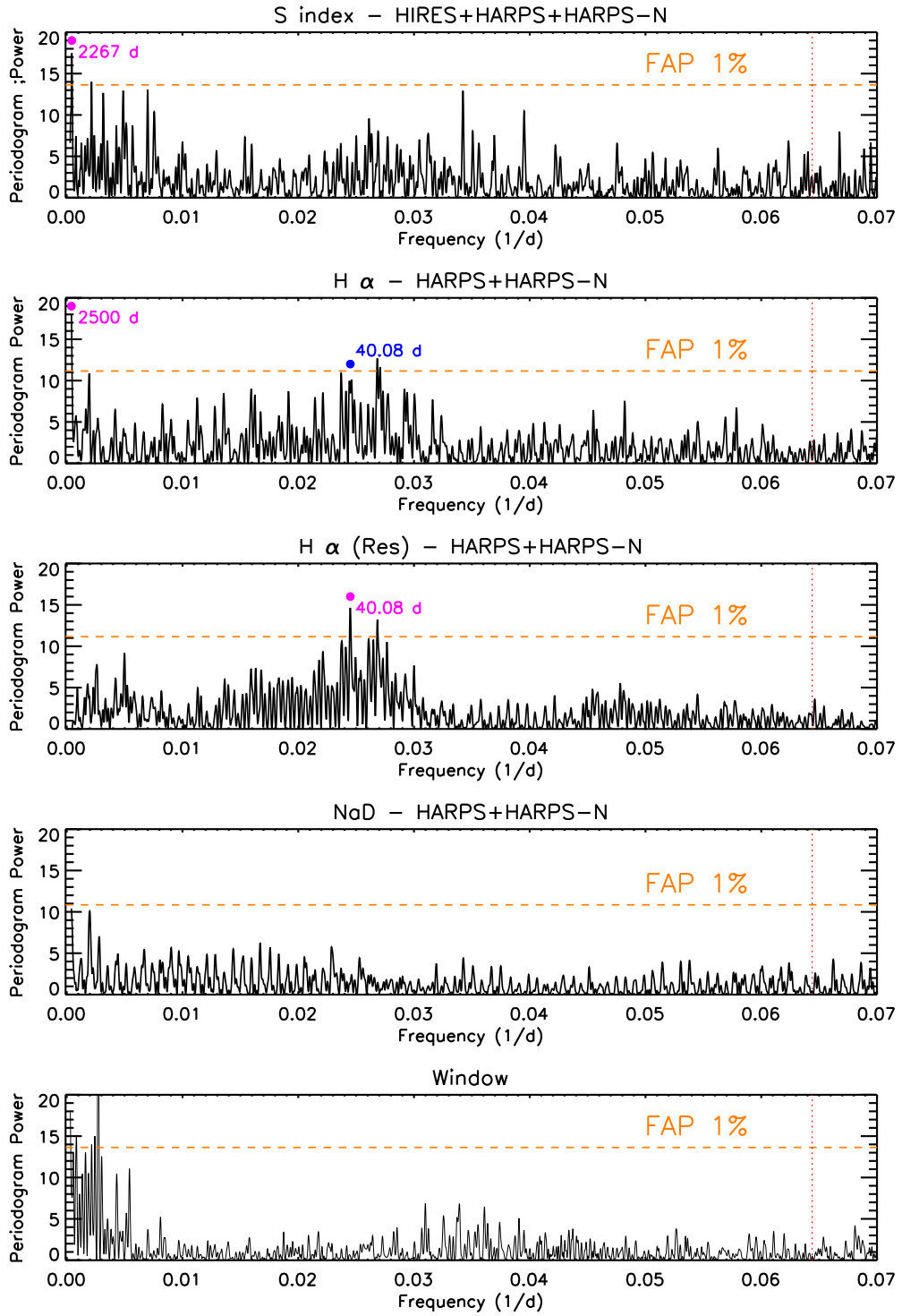


**Fig. A.4.** GLS periodograms of activity indexes (from top to bottom): Sindex (HIRES+HARPS+HARPS-N);  $H\alpha$  and NaD (HARPS+HARPS-N) and window function. The 15.5 d period is indicated in each periodogram, as the red dashed line. The significant periods discussed in Sect. 3.4, are indicated with a magenta dot. In the  $H\alpha$  periodogram (HARPS+HARPS-N), we also indicated, with a blue dot, the 40.8 d period which becomes significant in the residual time series, after the removal of the long 2500 d period.

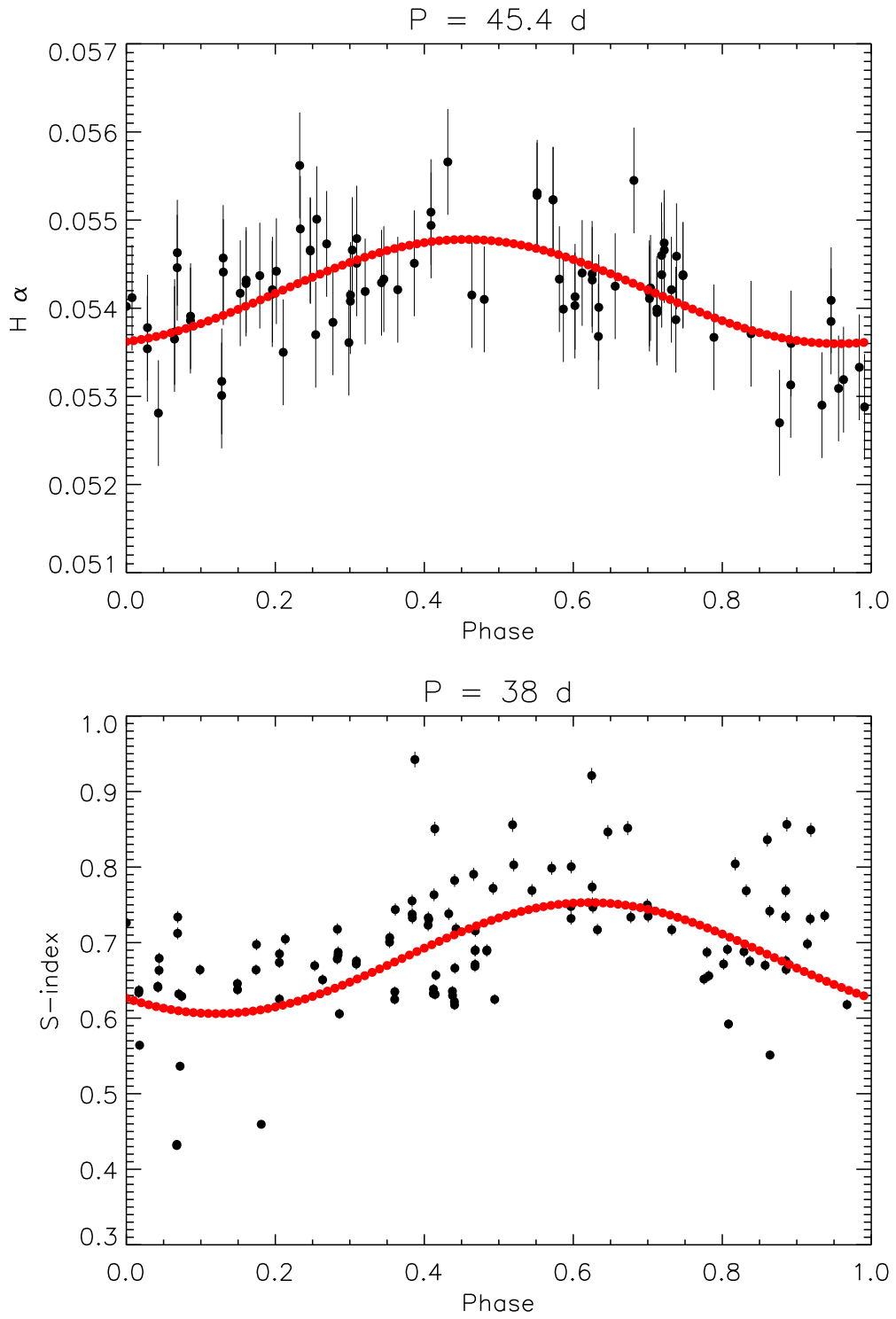


**Fig. A.5.** Upper panel:  $H\alpha$  data folded at the best period (HIRES, 114 data points). Lower panel: S-index data folded at the best period (HIRES, 114 data points). The red line is the best fit solution, in both panels.

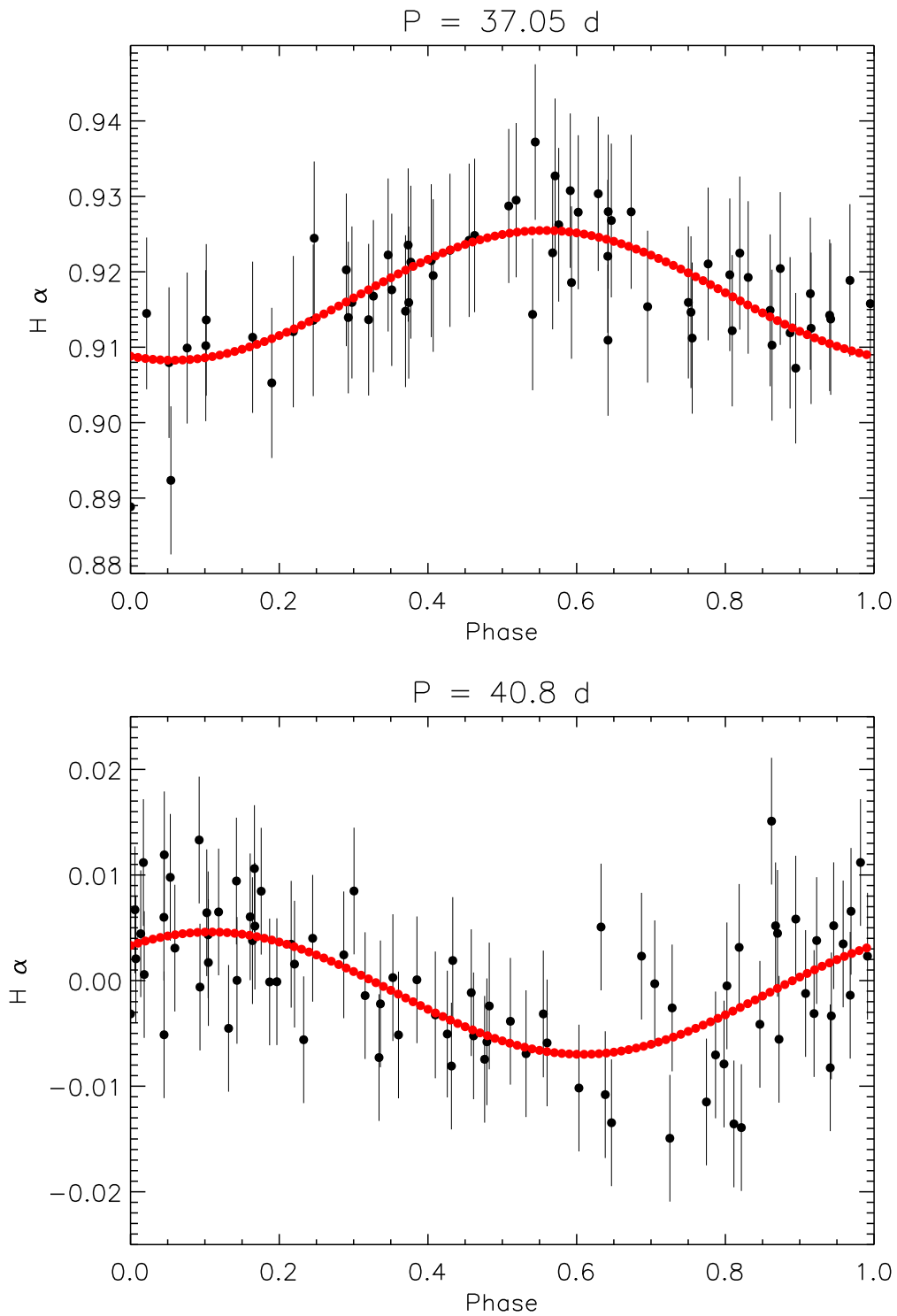


**Fig. A.6.** Upper panel:  $H\alpha$  data folded at the best period (HARPS-N, 64 data points). Lower panel:  $H\alpha$  residual data (HARPS + HARPS-N, 84 data points), after the subtraction of the 2500 d period, folded at the best period. The red line is the best fit solution, in both panels.